

PLANAR AND CYLINDRICAL RAYLEIGH–TAYLOR EXPERIMENTS ON NOVA (HEP2)

B. A. Remington

S. V. Weber

M. M. Marinak

W. W. Hsing

N. M. Hoffman

Introduction

A high-density fluid on top of a low-density fluid is Rayleigh–Taylor¹ (RT) unstable. Driven by gravity, random perturbations at the interface between the two fluids will grow: fingers (“spikes”) of the heavier fluid will poke through the lighter fluid, and bubbles of the lighter fluid will rise into the heavier fluid. The RT instability and its shock-driven analog, the Richtmyer–Meshkov² (RM) instability, have been a focus of research in inertial confinement fusion (ICF) for some time.^{3–19} In ICF, the driver—laser light, x rays, or ions—heats the outer layer of the capsule wall, causing it to ionize and expand rapidly. The result is a low-density ablated plasma accelerating the high-density capsule wall (“pusher”). The ablation front is RT unstable, and outer-surface imperfections grow. This growth can seed perturbations at the pusher inner wall, which in turn become RT unstable during deceleration and stagnation. Ultimately, pusher material can mix into the fuel, degrading performance.

The role of the RT instability in ICF can be understood heuristically as follows. The goal of ICF is to maximize the fuel core pressure P_{core} for a minimum applied (ablation) pressure P_a . To see how we might do this, we write²⁰

$$\frac{P_{\text{core}}}{P_a} = 10 \left(\frac{R_0}{\Delta R} + 1 \right) \left(\frac{R_0}{R_s} \right)^{0.9}, \quad (1)$$

where $R_0/\Delta R$ is the capsule aspect ratio (the ratio of initial shell radius to shell thickness) and R_0/R_s the convergence ratio [the ratio of outer capsule radius to final compressed hot fuel radius (the “hot spot” radius)]. The $[(R_0/\Delta R) + 1]$ factor results from converting the kinetic energy of the pusher into pressure at stagnation, by using Bernoulli’s theorem, i.e., $P_{\text{stag}} = P_a + (1/2) \rho v^2$. The $(R_0/R_s)^{0.9}$ factor results from the pressure multiplication due to the spherically imploding shock wave and is based on the self-similar solutions of Guderley.²⁰

From Eq. (1), we immediately see that maximum pressure amplification occurs for high-aspect-ratio capsules with a high convergence ratio.

The RT instability limits the aspect ratio, however, as we see from the following. In the linear regime, perturbation growth is exponential in time,

$$\eta = \eta_0 \int \gamma dt, \quad (2)$$

where the exponent $\int \gamma dt$ represents growth in terms of perturbation e -foldings. A dispersion curve for the RT growth rate γ can be written as⁸

$$\gamma \approx \left(\frac{kg}{1 + kL} \right)^{1/2} - \beta k v_a, \quad (3)$$

where $k = 2\pi/\lambda$ is the perturbation wave number, g is the pusher acceleration, $L = \rho/\Delta\rho$ is the density gradient scalelength at the ablation front, β is a multiplier usually set in the range of 1 to 3, $v_a = \dot{m}/\rho$ is the ablation velocity, \dot{m} is the mass ablation rate per unit area, and ρ is a characteristic density at the ablation front. If we assume (1) a constant acceleration over a distance $S \approx R_0/2$, (2) that 80% of the pusher is ablated over this distance ($\int v_a dt \approx 0.8\Delta R$), and (3) a density gradient scale length that is 10 to 20% of the shell thickness ($L = \alpha\Delta R$, with $\alpha = 0.1\text{--}0.2$), then we can approximate the perturbation e -foldings as

$$\int \gamma dt \approx \left(\frac{\ell}{1 + \alpha\ell \frac{\Delta R}{R}} \right)^{1/2} - 0.8\ell \frac{\Delta R}{R}. \quad (4)$$

Here we have substituted $k = \ell/R$, where ℓ is the mode number of a spherical harmonic. We have chosen $\beta \sim 1$ which is typical of indirect drive. When $\Delta R/R$ is small, Eq. (4) shows that the perturbation e -folding is large. One can maximize $R_0/\Delta R$, and hence the pressure

amplification, only to the extent that the RT growth will allow.

The situation for a capsule implosion, illustrated in Fig. 1, can be approximated as $G_T = G_1 f G_2$, where the total growth factor G_T has been decomposed into growth at the ablation front or outer surface G_1 , fractional feedthrough f to the inner surface or pusher–fuel interface, and growth at the inner surface G_2 . Experiments to measure mix (and hence G_T) directly in implosions are difficult, typically relying on spectroscopic tracer layers or yield degradation to signal the onset of mix.^{18,19} The dominant source for the total perturbation growth and subsequent mixing, however, is the growth G_1 of outer-surface perturbations during the acceleration phase. This can be measured directly with high precision with face-on experiments in planar geometry. The integral effect, namely, outer-surface growth, feedthrough, and inner-surface growth, can be measured with side-on imaging of cylindrical implosions. The HEP2 campaign comprises these two areas—planar and cylindrical RT experiments.

The evolution of a single-mode perturbation at the ablation front of an accelerated planar foil is expected to have three distinct phases. (1) When the drive first turns on, a strong shock is launched through the foil during compression. The shock front will typically be deformed, bearing the imprint of any initial surface imperfections. The behavior of this perturbed (or “rippled”) shock front is dynamically similar to that produced by the RM instability.² Material behind the shock develops a lateral velocity component, moving from regions in which the foil was thinner (initial perturbation valley) towards regions in which the foil was thicker (initial perturbation peak), increasing the areal density modulation. The shape of the shock front is not constant, but evolves with

time.^{21,22} The areal density modulation may decrease or even reverse phase, if the foil is thick enough with respect to the perturbation wavelength. (2) After the shock breaks out of the back of the foil (the side away from the drive), and a rarefaction wave returns to the ablation front, the compressed foil accelerates as a unit. Perturbation growth continues, now as a result of the RT instability. The linear regime is defined by $k\eta \ll 1$, where $k = 2\pi/\lambda$ represents the perturbation wave number and λ and η are the perturbation wavelength and spatial amplitude. In the linear regime, the perturbation grows exponentially as given in Eq. (2), namely, $\eta(t) = \eta_0 e^{\gamma t}$, where the growth rate γ can be written approximately as in Eq. (3) in the form of a dispersion curve,⁸

$$\gamma \approx \left(\frac{kg}{1 + kL} \right)^{1/2} - \frac{\beta k \dot{m}}{\rho}.$$

(3) After sufficient growth, $k\eta$ is no longer small and the perturbation enters the nonlinear regime. The shape of the perturbation changes from sinusoidal to “bubble and spike,” which corresponds in Fourier space to the generation of higher harmonics.⁷ Within the framework of third-order perturbation theory,²³ the amplitudes of the perturbation fundamental mode (first harmonic) η_1 , second harmonic η_2 , and third harmonic η_3 can be written as

$$\eta_1 \approx \eta_L \left(1 - \frac{1}{4} k^2 \eta_L^2 \right), \quad (5a)$$

$$\eta_2 \approx \frac{1}{2} k \eta_L^2, \quad (5b)$$

$$\eta_3 \approx \frac{3}{8} k^2 \eta_L^3, \quad (5c)$$

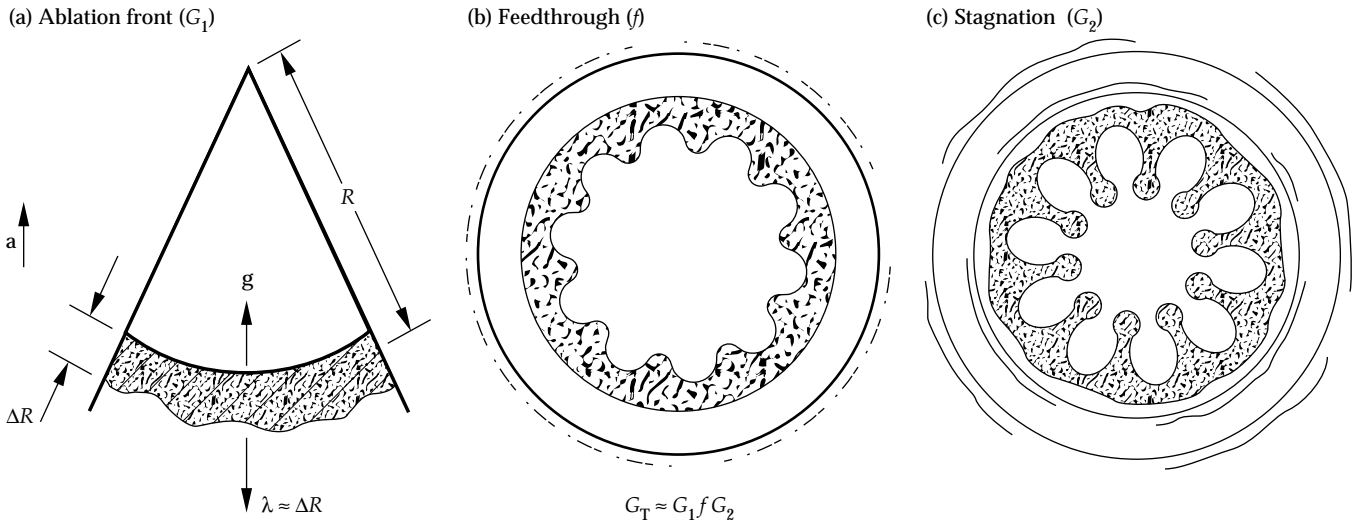


FIGURE 1. Schematic showing how RT perturbation growth affects an implosion. The quantities G_T , G_1 , f , and G_2 correspond to the total growth factor, growth factor at the outer surface during acceleration, feedthrough to the inner surface, and growth factor at the inner surface during deceleration. (20-03-1293-4392pb02)

where η_L is the linear-regime spatial amplitude given by Eq. (2). The wave numbers of the first three harmonics correspond to $k_n = 2\pi n/\lambda$, $n = 1, 2, 3$. At third order, we see in Eq. (5a) the occurrence of negative feedback to the first harmonic; that is, the growth of the fundamental is decreased. The perturbation growth is said to “saturate.” In the asymptotic limit of the nonlinear regime, the bubble amplitude can be written as

$$\eta(t) = \int (Fg\lambda)^{1/2} dt, \quad (6)$$

which corresponds to a perturbation growing at its terminal bubble velocity,²⁴

$$v_B = (Fg\lambda)^{1/2}, \quad (7)$$

where $F = u^2/gl$ is the dimensionless Froude number, which depends only on the shape of the perturbation (here u , g , and l are characteristic flow velocity, acceleration, and spatial scale, respectively). As derived by Layzer,²⁵ $F^{1/2} = 1/(6\pi)^{1/2} = 0.23$ in two dimensions (2-D) and 0.36 in three dimensions (3-D) for an axisymmetric bubble. If we define the transition into the nonlinear regime as taking place when the growth in the fundamental mode is reduced by 10%, then from Eq. (5a) we have $k^2\eta_L^2 = 0.1$, or $\eta_L/\lambda \approx 0.1$, which is a typical and widely used threshold for nonlinearity. This same transition criterion results if one assumes that the onset of nonlinearity occurs when the linear-regime perturbation velocity is equal to the asymptotic nonlinear bubble velocity, namely, $\dot{\eta} \approx v_B$, or $\gamma\eta = (kg)^{1/2}\eta = (g\lambda/6\pi)^{1/2}$. Rearranging again leads to $\eta/\lambda \approx 0.1$ at saturation.

In the nonlinear regime,^{26–31} mode coupling leads to the appearance of “beat” modes $k_i \pm k_j$. To second order, this can be written as

$$\eta_{k_i \pm k_j} \approx \mp \frac{1}{2} (k_i \pm k_j) \eta_{k_i}^L \eta_{k_j}^L; \quad (8)$$

Eq. (8) is derived in the Appendix. Mode coupling redistributes a multimode perturbation to longer and shorter wavelengths and affects the saturation of individual modes. If a perturbed interface has a sufficiently dense Fourier composition, it becomes convenient to think of the perturbation in terms of a characteristic wave number $k_{\text{char}} = 2\pi/\lambda_{\text{char}}$ and a characteristic spatial amplitude η_{char} . In these terms, the criterion for the onset of saturation becomes $k_{\text{char}}\eta_{\text{char}}$ no longer being small. Within a continuum model,³² this leads to *individual* constituent modes saturating when their amplitudes reach a threshold S_k given by

$$S_k = \frac{v_{2D}}{L^{1/2}k^{3/2}}, \text{ in 2-D} \quad (9a)$$

$$S_k = \frac{v_{3D}}{Lk^2}, \text{ in 3-D} \quad (9b)$$

where L represents the system size and v is a parameter determined by comparison with simulations or data.

We present here the results of an extensive, multiyear experimental and computational study of perturbation growth on planar foils and on imploding cylinders

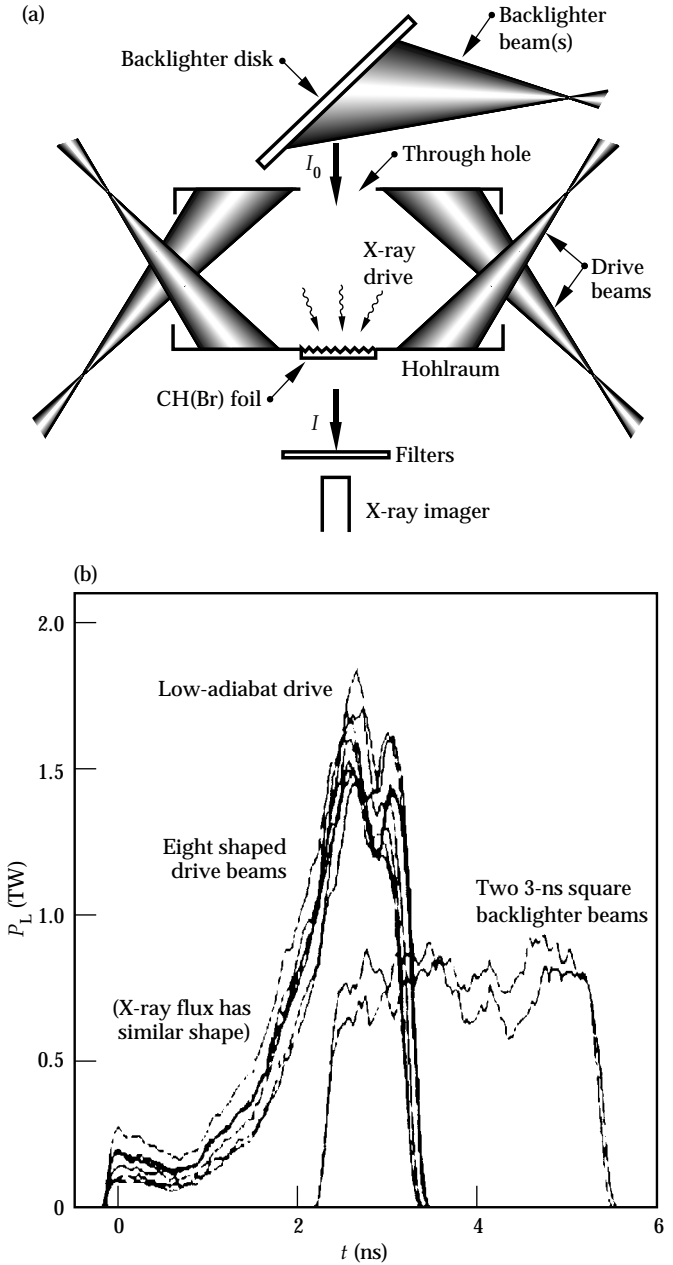


FIGURE 2. (a) The experimental configuration consists of a cylindrical Au hohlraum (3000 μm long, 1600 μm diam) with the modulated CH(Br) foil mounted on the wall. (b) In the hohlraum, eight $\lambda = 351\text{-nm}$ laser beams are converted to x rays, which ablatively accelerate the foil. Two additional laser beams at $\lambda = 528\text{ nm}$ generate backlighter x rays used for in-flight diagnosis of the foil. (20-03-1293-4392pb03)

driven with an x-ray drive. We investigated initial perturbations of the form

$$\eta(x) = \sum_{n=1}^m \eta_n \cos(k_n x),$$

where $k_n = 2\pi n/\lambda$, for $m = 1, 2$, and 8 . The modes are enumerated as harmonics of the longest repeating pattern. In the next section, we discuss the “Experimental Details,” and in “Drive Characterization” we present our drive characterization work. The following sections discuss “Single-Mode Experiments,” “Two-Mode Experiments,” and “Eight-Mode Experiments.” Our 3-D single-mode experiments and simulations are discussed in “3-D Single-Mode Experiments.” The cylindrical experiments are discussed in “The RT Instability in Cylindrical Implosions,” and conclusions are given in “Summary.” The final section, “Appendix: Amplitude of Coupled Modes,” discusses a second-order perturbation model.

Experimental Details

Figure 2 shows the experimental setup for the planar experiments using a shaped, low-adiabat drive. Sinusoidal surface perturbations are molded onto one side of a planar 750- μm -diam bromine-doped CH foil [$\text{C}_{50}\text{H}_{47}\text{Br}_{2.7}$, or “CH(Br)”] of density $\rho = 1.26 \text{ g/cm}^3$. A subset of the experiments were with fluorosilicone ($\text{SiOC}_4\text{H}_7\text{F}_3$ or “FS”, at $\rho = 1.28 \text{ g/cm}^3$). As shown in Fig. 2(a), the foil is mounted across a hole in the wall of

a 3000- μm -long, 1600- μm -diam cylindrical Au hohlraum with the perturbations facing inwards. The foil is diagnosed by back-illumination with an 800- μm -diam spot of x rays created by irradiating a backlighter disk with one or two $\lambda = 528\text{-nm}$ Nova³³ beams, typically delayed relative to the drive beams, as shown in Fig. 2(b). The modulations in foil areal density cause modulations in the transmitted backlighter x-ray flux, which are recorded as a function of time with gated or streaked x-ray imaging diagnostics. This is illustrated in Fig. 3 (taken from Refs. 14 and 15).

Instrumental spatial resolution is most conveniently expressed as the modulation transfer function (MTF), namely, the ratio of observed to actual contrast [$\Delta \ln E$, where E = film exposure]. The MTF for the 22 \times -magnification grazing-incidence Wölter x-ray microscope³⁴ used for most of these experiments is given by^{35–37}

$$M(k) = \frac{1}{1 + (k\sigma)^2}, \quad (10)$$

with $\sigma = 6.65 \mu\text{m}$; Fig. 4(a) shows M vs perturbation wavelength. The inverse Fourier transform of $M(k)$ corresponds to an exponential resolution function,

$$R(x) = e^{-x/\sigma}. \quad (11)$$

Figure 4(a) also shows a curve corresponding to Eq. (10) with $\sigma = 8.1 \mu\text{m}$; this is the lowest MTF that is consistent with the data.

Equations (10) and (11) correspond to the “top” sector of the Wölter microscope, which was used for most of the shots in this work. The “west” sector was used in one experiment; its resolution (which is slightly worse than that of the top sector) is given by

$$R(x) = \frac{1}{1 + \alpha} \left[\exp(-x/\sigma_1) + \alpha \exp(-x/\sigma_2) \right], \quad (12)$$

with $\alpha = 0.22$, $\sigma_1 = 3.5 \mu\text{m}$, and, $\sigma_2 = 18 \mu\text{m}$. Table 1 gives the correspondence between experiment and Wölter sector used. Figure 4(b) shows the MTF for one of the gated x-ray pinhole cameras used for some of these experiments, the FXI.³⁸ This camera was run at 8 \times magnification with 10- μm pinholes.

The Wölter microscope is a grazing-incidence x-ray optic, so it has a high-energy cutoff in its reflectance. We measured this cutoff on an identical second Wölter optic,³⁶ as illustrated in Fig. 5. The solid curve in Fig. 5(a) gives the x-ray emission spectrum resulting from electron-beam excitation of a cold Nb target at 5 keV. The dotted curve represents the same spectrum after double reflection off the x-ray optic. The ratio of these two curves (dotted/solid) gives the reflectance, shown in Fig. 5(b). The high-energy cutoff is at $\sim 3 \text{ keV}$; the peak reflectance is only about 10%. The smooth dashed curve in Fig. 5(b) is the theoretical double-bounce

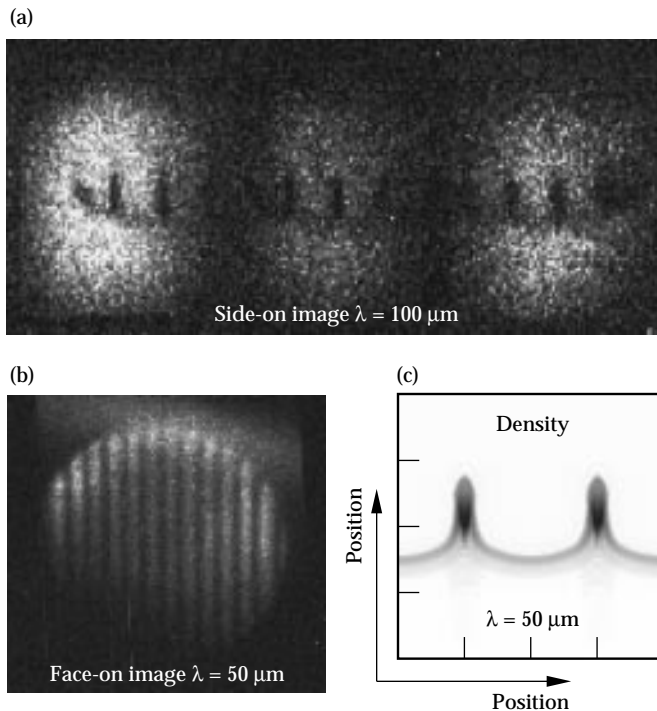


FIGURE 3. Sample images taken (a) in side-on geometry, (b) in face-on geometry, and (c) from 2-D simulations for planar experiments with FS foils. (20-03-1293-4393pb01)

reflectance of an ideal Ni surface at grazing angles of 1.1° and 1.2° , multiplied by an overall degradation factor of 0.3, and represents the reflectance assumed in the post-processing of the simulations for these experiments. The degradation factor is presumably caused by surface roughness and absorption by contaminants that have settled onto the Wölter optic surface.

Figure 6 shows the measured (time-integrated) spectra for Mo, Rh, and Sc, the backlighter materials used in the face-on experiments. On separate shots, the

backlighter disks were irradiated with 528-nm light at $I \approx 1 \times 10^{14} \text{ W/cm}^2$. The Mo spectrum [Fig. 6(a)] is dominated by $n = 3 \rightarrow 2$ L-band emission at 2.4–2.8 keV; the Rh spectrum [Fig. 6(b)] is also dominated by $n = 3 \rightarrow 2$ L-band emission, here at 2.8–3.3 keV. The Sc spectrum [Fig. 6(c)] is dominated by the $n = 2 \rightarrow 1$ He $_{\alpha}$ K lines. These backlighter materials were chosen by considering the total optical depth (OD) of the experimental foils and the response of the recording instruments.

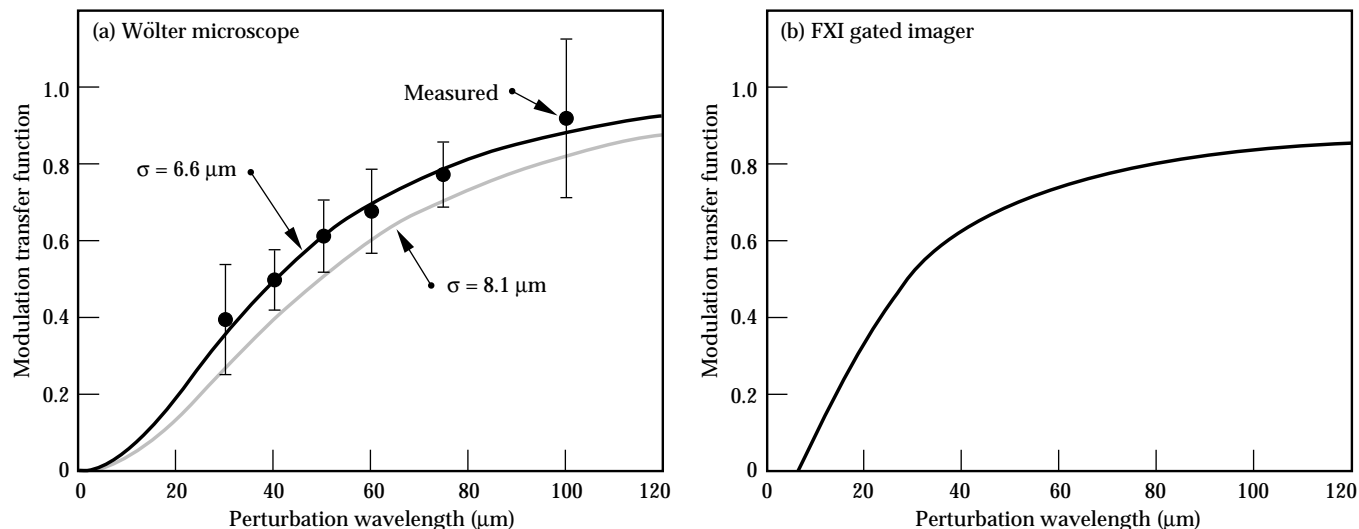


FIGURE 4. (a) Instrument modulation transfer function (MTF) vs perturbation wavelength for the 22 \times -magnification grazing-incidence Wölter x-ray microscope. The data points represent the measured MTF from the observed $t = 0$ contrast from accelerated rippled-foil targets. The data points and error bars for the $\lambda = 50 \mu\text{m}$ and $\lambda = 75 \mu\text{m}$ perturbations correspond to the means and standard deviations of the deduced MTF from seven and nine separate rippled-foil shots, respectively. The other data points correspond to single shots at each wavelength, and the error bars correspond to the standard deviation assuming that each individual period is independent data. The black curve represents a best fit of the data with the function $M(k) = 1/[1 + (k\sigma)^2]$, with $\sigma = 6.65 \mu\text{m}$; the gray curve is $M(k)$ for $\sigma = 8.1 \mu\text{m}$. (b) MTF for the FXI gated imager at 8 \times magnification with 10- μm pinholes and a Sc backlighter. (20-03-0394-0738pb03)

TABLE 1. Compilation of the data for each face-on single-mode shot, using the Wölter x-ray microscope. The ten columns in order give (1) foil material, (2) drive pulse shape, (3) perturbation wavelength, (4) the perturbation initial amplitude, (5) the foil thickness, (6) the total laser energy, (7) the sector (top or west) of the Wölter microscope used, (8) the backlighter material used, (9) the observed growth factor, and (10) the predicted growth factor from the LASNEX simulations.

Single-mode									
Foil	Drive	λ (μm)	η_0 (μm)	Thk (μm)	E_{Laser} (kJ)	Sector	Back-lighter	G_{obs}	G_{LASNEX}
CH(Br)	Shaped	100	2.4	48	16.1	Top	Rh	3.8	5.8
CH(Br)	Shaped	70	2.4	50	18.5	Top	Rh	6.5	7.3
CH(Br)	Shaped	50	0.42	57	17.4	West	Mo	19.9	24.0
CH(Br)	Shaped	30	1.5	53	15.1	Top	Rh	7.2	9.7
FS	Shaped	50	4.5	57.5	19.3	Top	Rh	6	4
FS	Shaped	50	0.8	56.0	16.6	Top	Rh	22	20
FS	Shaped	50	0.16	65.5	16.7	Top	Rh	75	75
FS	1 ns sq.	50	2.2	34.2	13.4	Top	Dy	2.9	2.8
CH	1 ns sq.	50	2.5	59.4	13.9	Top	U	1.7	1.9

Drive Characterization

Figure 7 shows the low-adiabat x-ray drive used in most of these experiments.^{14,15,37} This drive was generated by focusing eight 351-nm, 2.0–2.4-kJ, 3.3-ns temporally shaped Nova beams into the hohlraum, where they are converted to approximately thermal x rays. The black curve shows the total power of the eight laser beams on a typical shot. The intensity during the first 1.6–1.8 ns of the drive, called the “foot,” is about a factor of 10 lower than in the 16-TW peak, which occurs at 2.6 ns. This shaped pulse leads to a lower adiabat and higher compression than if the same total laser energy were delivered in a square pulse. The x-ray drive used in our analysis results from a two-

dimensional (2-D) hohlraum simulation³⁹ using the experimental laser power P_L , and is shown as radiation temperature $T_R(t)$ by the gray curve in Fig. 7. This x-ray drive has been checked by two independent experimental techniques: (1) shock breakout trajectory through an Al wedge mounted on the hohlraum and viewed with a streaked UV imager,⁴⁰ and (2) accelerated-foil trajectory using streaked side-on radiography.^{14,37} The resulting T_R profile has a ~95-eV foot increasing to 200 eV in the peak at about 3 ns. This shape mimics, on a short time scale, the early stages of an ignition pulse shape, which typically has a ~90-eV foot followed by a stepped ramp to a 300-eV peak.⁴¹

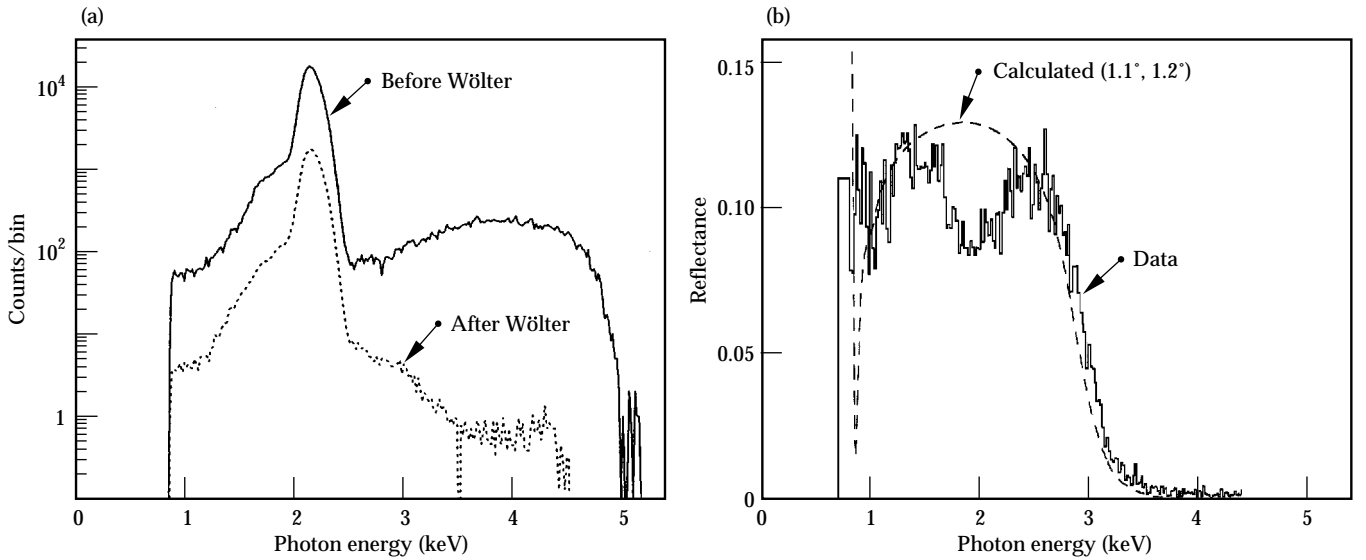


FIGURE 5. Measured Wörlter reflectivity vs x-ray energy. In (a) the solid curve corresponds to the x-ray emission spectrum from a Nb transmission target bombarded by a focused electron beam accelerated across a potential difference of 5 kV. The dotted curve is the same except the x rays have undergone two $\sim 1^\circ$ grazing-incidence reflections off the Ni surface of the Wörlter x-ray optic. (b) The solid histogram gives the ratio (dotted/solid) of the two curves in (a) and corresponds to the Wörlter reflectance. The smooth dashed curve represents the calculated reflectance for two ideal Ni surfaces at grazing angles of 1.1° and 1.2° , with an overall degradation factor of 0.3. (20-03-0394-0740pb02)

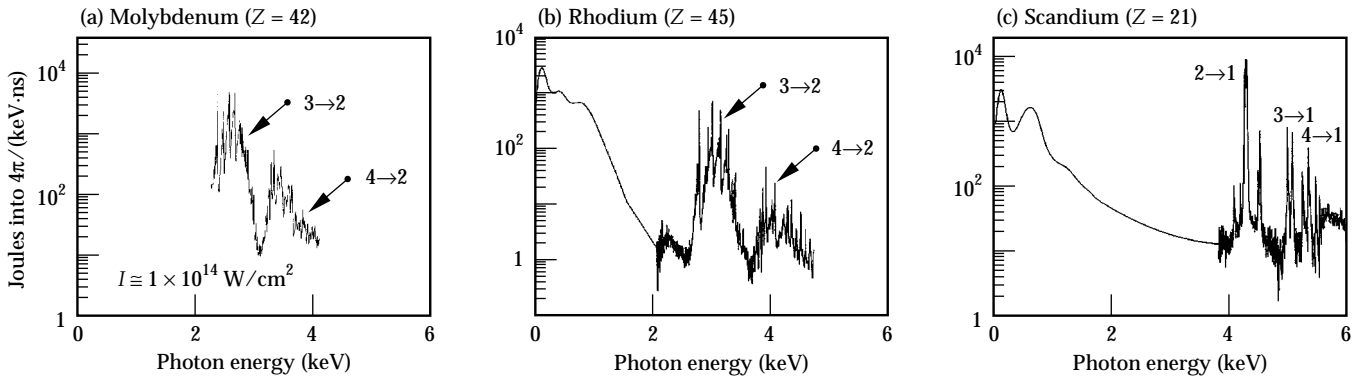


FIGURE 6. Time-integrated spectra for the backlighters used in the face-on experiments. In each case, a single 5-ns laser beam ($\lambda = 528$ nm, $I \approx 1 \times 10^{14}$ W/cm²) was used. The backlighter disks were (a) Mo, (b) Rh, and (c) Sc. The dominant transitions are marked. The high-energy portion of each spectrum was measured with a static crystal (RAP) spectrometer, and the low-energy portions with a filtered photodiode array. (20-03-0394-0739pb02)

Figure 8 shows the drive spectrum during the foot and at peak power for the nominal conditions of this investigation. For comparison we also show Planckian spectra corresponding to radiation temperatures $T_R = 95$ eV during the foot and $T_R = 200$ eV during the peak. The actual drive spectrum used derives from a full hohlraum simulation,³⁹ but is not too different from the time-dependent combination of a Planckian with the spectrum

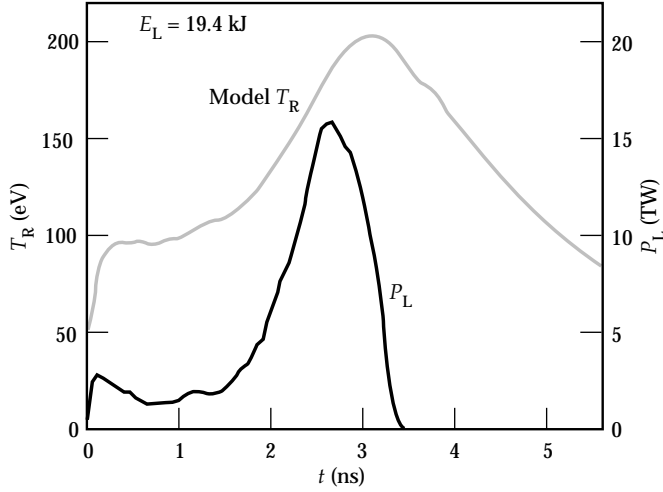


FIGURE 7. Drive expressed in terms of laser power and x-ray radiation temperature. Black curve (scale on right) gives total power vs time of the eight $\lambda = 351$ -nm drive laser beams. The adopted drive temperature $T_R(t)$, shown by the gray curve (scale on left), was obtained from a 2-D hohlraum simulation. The first 2 ns represents the “foot”; peak laser power P_L occurs at 2.6 ns; peak T_R occurs at 3 ns. (20-03-1293-4397pb02)

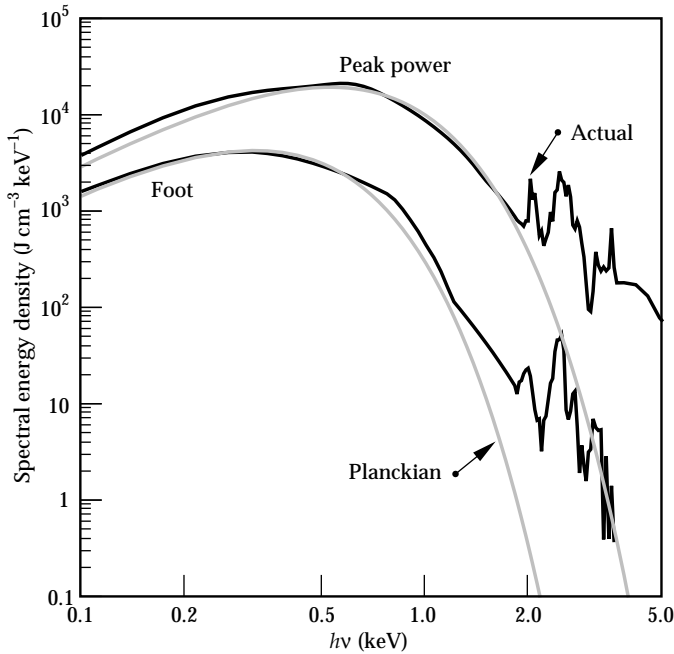


FIGURE 8. Black curves represent nominal drive spectra during the foot and the peak of the drive shown in Fig. 7. Gray curves correspond to Planckian spectra at $T_R = 100$ and 200 eV. (20-03-0394-0743pb02)

from a planar Au disk illuminated by a shaped $\lambda = 351$ -nm laser pulse. The weighting of the two spectra for this case (shown in Fig. 8) corresponds to the relative solid angles subtended by the foil mounted on the hohlraum wall for the eight laser spots in the hohlraum versus that for the wall area not directly illuminated with laser light. The contribution of the Au M-band emission from the laser spots causes the drive spectrum to be “harder” than a Planckian spectrum.

From the strong-shock relations for ideal fluids,⁴² the shock-front velocity v_s and pressure P behind the shock front are related by $P \approx \rho_{us} v_s^2$, where ρ_{us} is the density of the unshocked material. From Ref. 43 we can write $P \propto T_R^{7/2}$, so we have $T_R \propto P^{2/7} \propto v_s^{4/7}$. When applied to Al, for example, and after correcting for albedo effects, this becomes⁴⁰

$$T_R = \frac{v_s^{0.63}}{80}, \quad (13)$$

with T_R in eV and v_s in cm/s; the numerical factor arises from the equation of state (EOS) of Al. A

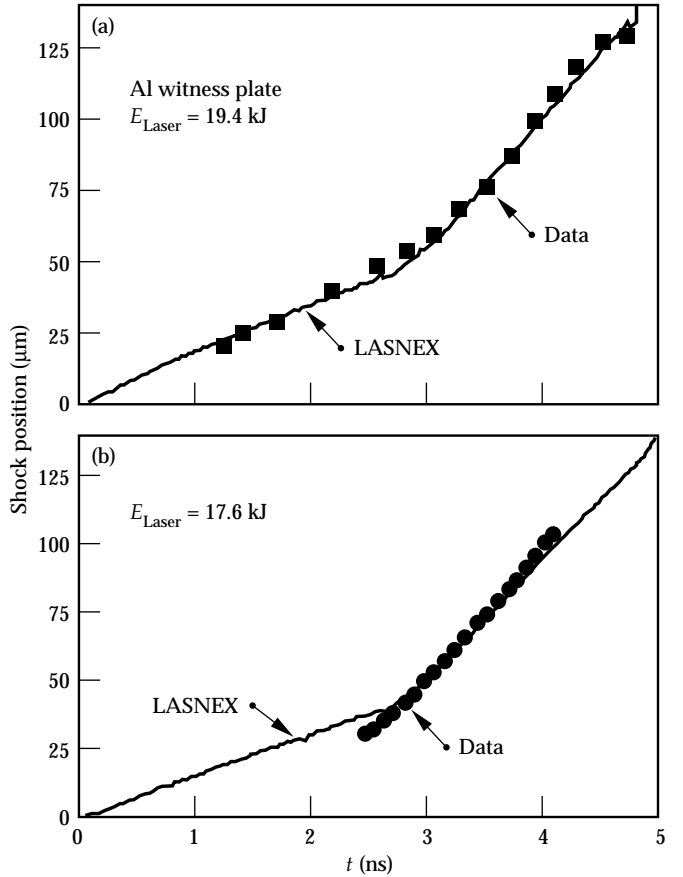


FIGURE 9. The drive is characterized with measurements of shock trajectory, deduced from measuring in face-on geometry the shock breakout time across a variable-thickness Al wedge mounted on the wall of the hohlraum. Corresponding 1-D LASNEX simulations are shown. (a) Results for 19.4-kJ shot discussed in Figs. 7 and 8. (b) Results for $E_{\text{Laser}} = 17.6$ kJ. (20-07-0394-0744pb03)

measurement of shock velocity therefore allows us to deduce the ablation pressure and drive temperature.

Figure 9 shows measured shock trajectories for two shots. The measurements were made by viewing a wedged Al witness plate face-on with a streaked UV imager.⁴⁰ The shock breakout time is recorded as a function of position across the increasing thickness of the witness plate, allowing the shock trajectory to be reconstructed. Figure 9 shows the experimental trajectories at two laser energies and the corresponding simulations from 1-D LASNEX⁴⁴ using the drive described above (scaled in proportion to the laser power history for the lower-energy shot). The absolute timing of the shock trajectory data relative to drive turn-on ($t = 0$) was experimentally determined in the data shown in Fig. 9(b) but not in Fig. 9(a), where only the relative time was measured. The agreement between the data and simulation is very good. The data for the higher-energy shot [Fig. 9(a)] and the simulations for both shots show a two-component trajectory corresponding to an initial shock launched by the foot, and a delayed second shock coming from the peak of the drive. For the measured two-shock system in Fig. 9(a), the first shock has a velocity $v_1 \approx 20 \mu\text{m/ns}$, and the second shock has a peak velocity of $v_2 \approx 53 \mu\text{m/ns}$. The simulations give velocities of 16 and $46 \mu\text{m/ns}$, respectively. Applying Eq. (13) directly to the data gives $T_R \approx 120$ and 215 eV for the foot and peak of the drive, as compared to 100 and 200 eV from the simulations.

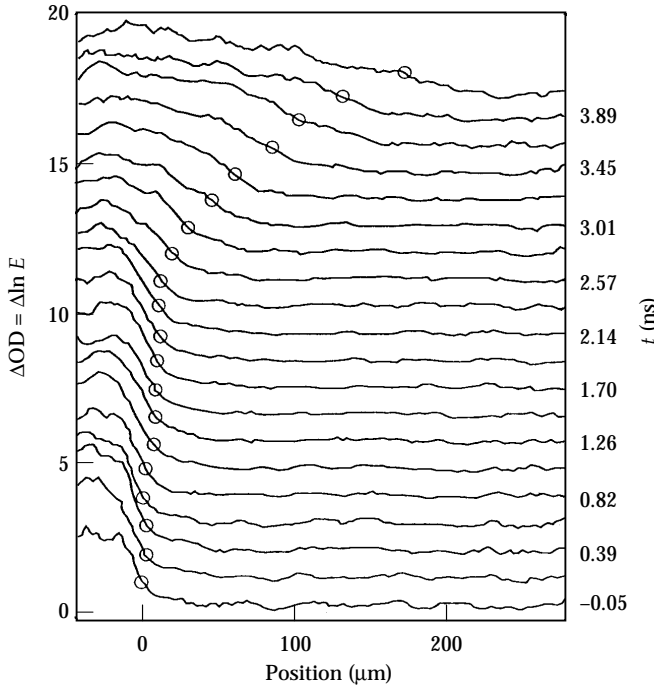


FIGURE 10. Foil trajectory (for a FS foil) in side-on geometry measured with the Wölter x-ray microscope. The profiles are of optical depth OD, and are artificially offset vertically by time, as indicated on the right-hand vertical axis. The circles represent the position that was taken as the foil rear edge (side away from x-ray drive). (20-03-0895-2047pb01)

The foil trajectory, which is a measure of the gross hydrodynamics, was obtained by viewing across the rear edge of the foil in side-on geometry,^{14,15} as shown in Fig. 10. This trajectory is reproduced very well with the 1-D simulation using the drive model described above, as illustrated in Fig. 11 for a CH(Br) foil. The back edge of the foil does not begin to move until shock breakout at $\sim 2.6 \text{ ns}$. The foil then accelerates during the interval $2.6 \leq t \leq 3.6 \text{ ns}$, after which the drive is turning off and the foil begins to coast. The black curve represents the foil trajectory from the 1-D LASNEX simulation; the gray curve represents the acceleration of the ablation front, defined as the zone of half peak density. The fluctuations in the acceleration at 0.2 and 2.2 ns are due to the passage of the first and second shocks. The inset in Fig. 11 gives the ablation velocity $v_a = \dot{m} / \rho_{\text{max}}$ and density gradient scalelength $L = \rho / \nabla \rho$ where \dot{m} is the mass ablation rate per unit area, ρ_{max} is the peak density, and ρ and $\nabla \rho$ are the density and its gradient. (Computationally, the scalelength L is taken as the minimum value of $[\partial(\ln \rho) / \partial z]^{-1}$). Calculations based on this drive give better agreement with experiment than was obtained in preliminary results.⁴⁵

It is instructive to look in more detail at the effect of this shaped drive on the foil. Figures 12(a)–12(c) show results from the 1-D LASNEX simulations for radiation drive temperature, ablation pressure (defined as peak pressure in the simulation), and foil peak density as functions of time. Figures 12(d)–12(f) give the corresponding spatial profiles of electron temperature $T_e(z)$, pressure $P(z)$, and density $\rho(z)$ at five times spanning

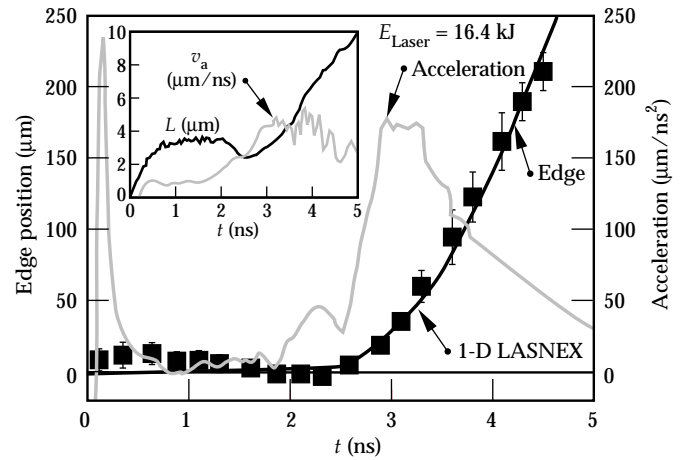


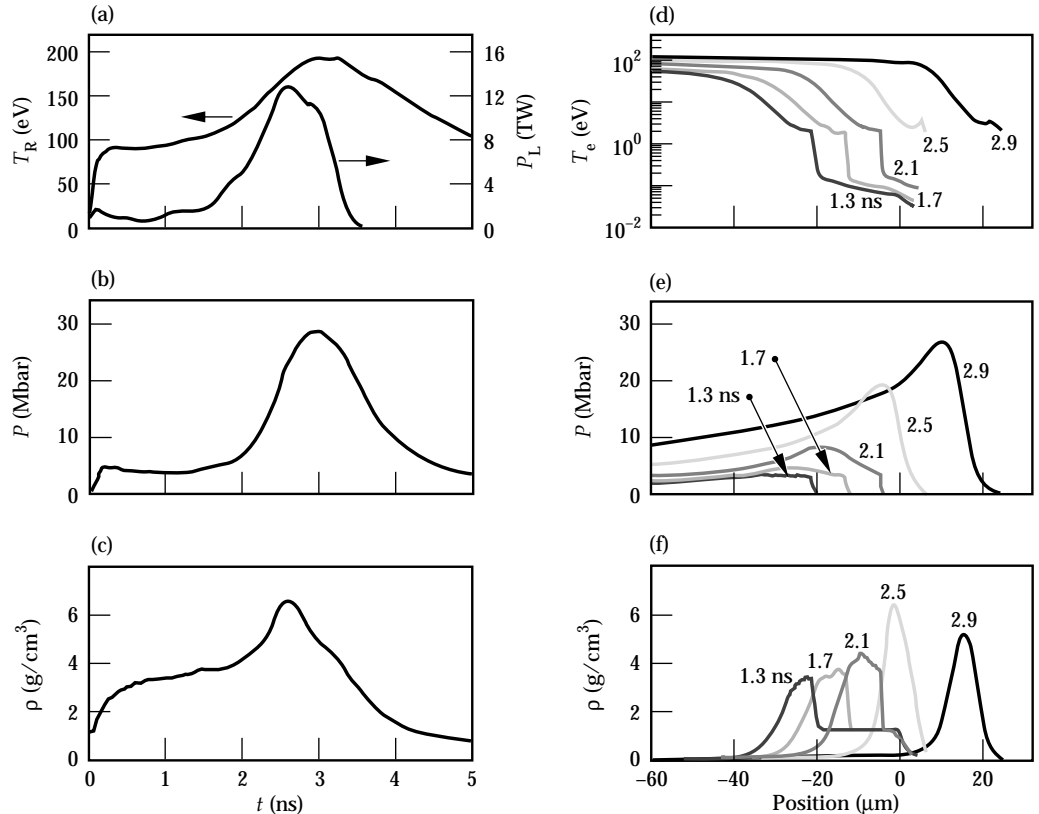
Figure 11. The square plotting symbols represent the measured position of the rear edge (side away from the x-ray drive) of the foil as a function of time. These data represent the average of two shots, one using a $50\text{-}\mu\text{m}$ -thick and the other a $48\text{-}\mu\text{m}$ -thick CH(Br) foil. Error bars represent uncertainties in defining the edge of the foil. The black curve represents the result of the 1-D LASNEX simulation. The rear edge of the foil does not start to move until after shock breakout at 2.6 ns . The gray curve represents the acceleration of the ablation front (defined as the zone of half peak density). Inset: ablation velocity and density gradient scalelength from the simulation. (20-07-0592-1702Bpb02)

1.3–2.9 ns. In Fig. 12(a), the drive $T_R(t)$ shows a ~ 90 -eV foot for the first 1.5 ns, an increase to a peak of 190 eV at 3 ns, and a decay to ~ 100 eV at 5 ns. The resulting ablation pressure in the CH(Br) foil (Fig. 12b) shows a 3–5 Mbar foot and a peak of 28 Mbar at 3 ns, i.e., at the same time as the peak in T_R . [This is also the time of peak acceleration and peak ablation velocity (Fig. 11).] The peak density of the foil [Fig. 12(c)] is generated just behind the strongest shock, reaching 6.5 g/cm^3 or a compression of 5.2 at 2.6 ns, when the second shock breaks out of the back of the foil and is at maximum strength. (This is also the time of minimum L , shown in the inset in Fig. 11.) The $T_e(z)$ profile at 1.3 ns [Fig. 12(d)] shows a sharp increase at $z = -20 \text{ }\mu\text{m}$ because of the passage of the first shock. Notice, however, that a low level of heating precedes the first shock ($z > -20 \text{ }\mu\text{m}$). This “preheat” results from the deep penetration of the hard component ($h\nu \gtrsim 1.4 \text{ keV}$) of the drive spectrum. By 2.5 ns, the second shock has overtaken the first, and the sharp features in $T_e(z)$ are washed out. The pressure profiles [Fig. 12(e)] convey a similar picture. During the interval 1.3–2.1 ns, the sharp rise in pressure to 4 Mbar due to the first shock is readily apparent. At 2.5 ns, the second shock has overtaken the first, increasing the pressure to 20 Mbar, and at 2.9 ns the pressure reaches its maximum of 28 Mbar. Figure 12(f) shows the effect on the foil compression of this staged two-shock drive. The compression at 1.3 ns just behind the first shock increases the foil density from 1.26 to 3.3 g/cm^3 . By the time the second shock has overtaken the first at 2.5 ns, the peak

density has reached 6.4 g/cm^3 , corresponding to a compression of 5. This is greater than the maximum possible compression of 4 for a single strong shock (in the ideal-gas limit). The staging of multiple shocks allows a higher compression by maintaining the foil on a lower adiabat.

We illustrate the lower adiabat achievable with this shaped drive by characterizing an adiabat with the ratio $\alpha = P/P_{\text{FD}}$ of pressure at peak density to that of a Fermi-degenerate gas at the same density (which represents the lowest possible internal energy). For P_{FD} , we use the pressure at zero temperature for the EOS of the foil. For the low-adiabat drive shown in Fig. 12, we have $\alpha \approx 2$; for a 1-ns square drive at the same laser energy¹³ we have $\alpha \approx 9$, a factor of 4.5 higher. Note that the EOS for a real material differs significantly from that of an ideal Fermi fluid for densities only a few times solid density. The value of the parameter α defined above does not uniquely characterize an isentrope but changes with density along one. The value of α goes to infinity at solid density because $P_{\text{FD}} \rightarrow 0$. The value of α does, however, approach a constant along an isentrope in the limit $\rho \rightarrow \infty$. This asymptotic limit of α is about 1.25 for our low-adiabat drive, but it is 2.3 for a 1-ns square drive. Thus, if the foil driven with the shaped pulse were to be compressed to high density without introducing additional entropy, as in a capsule implosion, its compression would be close to that expected in the degenerate limit.

FIGURE 12. Various representations of the 16.4-kJ drive corresponding to results shown in Fig. 11 from 1-D simulations to illustrate the effect of pulse shaping. (a) Laser power P_L and radiation temperature T_R vs time. (b) Ablation pressure (defined as the peak pressure in the simulation) vs time. (c) Peak density vs time. (d)–(f) Spatial profiles of (d) electron temperature T_e , (e) pressure in the foil, and (f) foil density at 1.3, 1.7, 2.1, 2.5, and 2.9 ns, spanning the foot through the peak of the drive. The $0\text{-}\mu\text{m}$ position corresponds to the initial position of the back edge of the foil (the side away from the drive). The drive is incident from the left (negative) side. (20-03-0794-2831pb04)



Single-Mode Experiments

Figure 13 shows the data from a single-mode face-on experiment with a $\lambda = 100 \mu\text{m}$, $\eta_0 = 2.4 \mu\text{m}$ initial perturbation on a $48 \mu\text{m}$ thick CH(Br) foil.³⁷ Figure 13(a) shows the “raw” image; Fig. 13(b) shows profiles of modulations in optical depth $\Delta\text{OD} \approx -\ln E$ at early, intermediate, and late times. The initial perturbation amplitude was large, and we observe clear sinusoidal contrast (ΔOD) even at the earliest time, 0.2 ns. At 2.2 ns, the contrast is slightly greater and still sinusoidal, indicating that the growth is still in the linear regime. At 4.2 ns, the shape of the perturbation has deviated substantially from sinusoidal, forming sharp spikes and bubbles of high and low OD, respectively; the perturbation has entered the nonlinear regime. The transition from the linear to nonlinear regime is particularly clear in Fourier space; Fig. 13(c) shows the real components of the Fourier transform for the three ΔOD profiles. At 0.2 ns, only the η_1 fundamental mode (first harmonic) exists, indicating a purely sinusoidal perturbation. At 2.2 ns, η_1 has grown slightly but is still the only component, indicating a purely sinusoidal shape and linear regime. At 4.2 ns, a whole spectrum of higher Fourier harmonics—up to the fifth—is observed, corresponding to the bubble-and-spike shape of the top lineout in Fig. 13b. The perturbation is fully into the nonlinear regime.

Figure 14 shows the results of our λ -scaling experiments with single-mode CH(Br) foils. The data points represent the observations for the fundamental and the second harmonic. The error bars represent the standard deviation of the ensemble formed by treating each

individual period of the perturbations as independent data. The solid curves are the corresponding 2-D LASNEX⁴⁴ simulations. The $\lambda = 100 \mu\text{m}$ data shown in Fig. 14(a) is the full time evolution of the results shown at three particular times in Fig. 13. The perturbation growth evolves through three stages. Before shock breakout ($t < 2.5 \text{ ns}$), the perturbation is growing only slowly because of the rippled shock dynamics.^{21,22} For a brief period after shock breakout ($2.5 \text{ ns} \leq t \leq 3.2 \text{ ns}$) the perturbation is growing strongly because of the RT instability in the linear regime. Late in time ($t > 3.2 \text{ ns}$), the perturbation “saturates.” The evolution has entered the nonlinear regime, the second harmonic appears, and the observed contrast rolls over. The growth factor G , defined as the ratio of peak to initial contrast, was small here— $G = 4$. A similar situation occurs for $\lambda = 70 \mu\text{m}$, $\eta_0 = 2.4 \mu\text{m}$ [Fig. 14(b)]. Here, the overall growth was slightly greater, $G = 6$, reflecting the higher growth rate. For $\lambda = 50 \mu\text{m}$, $\eta_0 = 0.4 \mu\text{m}$ [Fig. 14(c)], the situation is qualitatively different. Because the initial amplitude is small, the perturbation evolution remains primarily in the linear regime, achieving the higher growth $G = 20$. Figure 14(d) shows the results for $\lambda = 30 \mu\text{m}$, $\eta_0 = 1.5 \mu\text{m}$. Because of the low instrumental MTF at $\lambda = 30 \mu\text{m}$ (see Fig. 4), the contrast remains low and no higher harmonics are observed. The observed growth factor for the fundamental mode was $G = 7$. Table 1 lists the key parameters for these experiments, including observed and simulated growth factors.

The solid curves in Fig. 14 represent the corresponding results from 2-D LASNEX simulations, after convolution

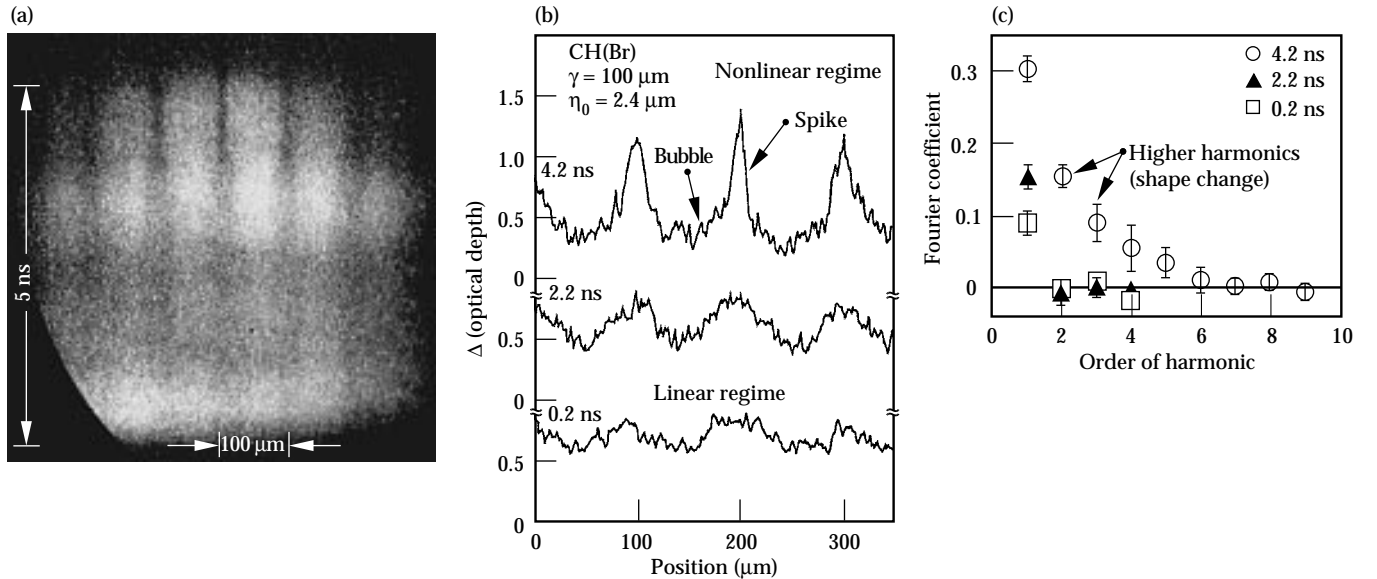


FIGURE 13. Various representations for single-mode face-on data for a $\lambda = 100 \mu\text{m}$, $\eta_0 = 2.4 \mu\text{m}$ perturbation imposed on a $48\text{-}\mu\text{m}$ -thick CH(Br) foil. (a) The “raw” streaked image is shown as film density. The film response is removed using a calibrated exposure across a precision P20 optical density wedge. (b) Profiles of $\Delta(\text{optical depth}) \approx -\ln E$ at 0.2, 2.2, and 4.2 ns. (c) Real components of the Fourier transforms for the profiles in (b). At late time, the perturbation enters the nonlinear regime, and up to the fifth harmonic of the perturbation Fourier composition is observed. (20-03-0394-0748pb02)

of the simulated image exposure with the instrumental resolution function [Eq. (11)]. (Our modeling is discussed in detail in Ref. 45.) Qualitatively, the simulations agree quite well with the data. There is modest growth dur-

ing the shock transit phase, strong growth after shock breakout, and then saturation with the appearance of the second harmonic, indicating entry into the nonlinear regime.

FIGURE 14. Results from single-mode, λ -scaling series for various values of λ and η_0 . Data points represent first harmonic (fundamental mode) and second harmonic Fourier coefficients of $\ln E$. Solid curves are corresponding results from 2-D LASNEX simulations. (a) Shows full time dependence for data of Fig. 13. All shots except that in (c) used the “top” sector of the 22 \times and a Rh backlighter; in (c), the west sector was used, and a Mo backlighter was used for slightly improved contrast. (20-03-0394-1063pb02)

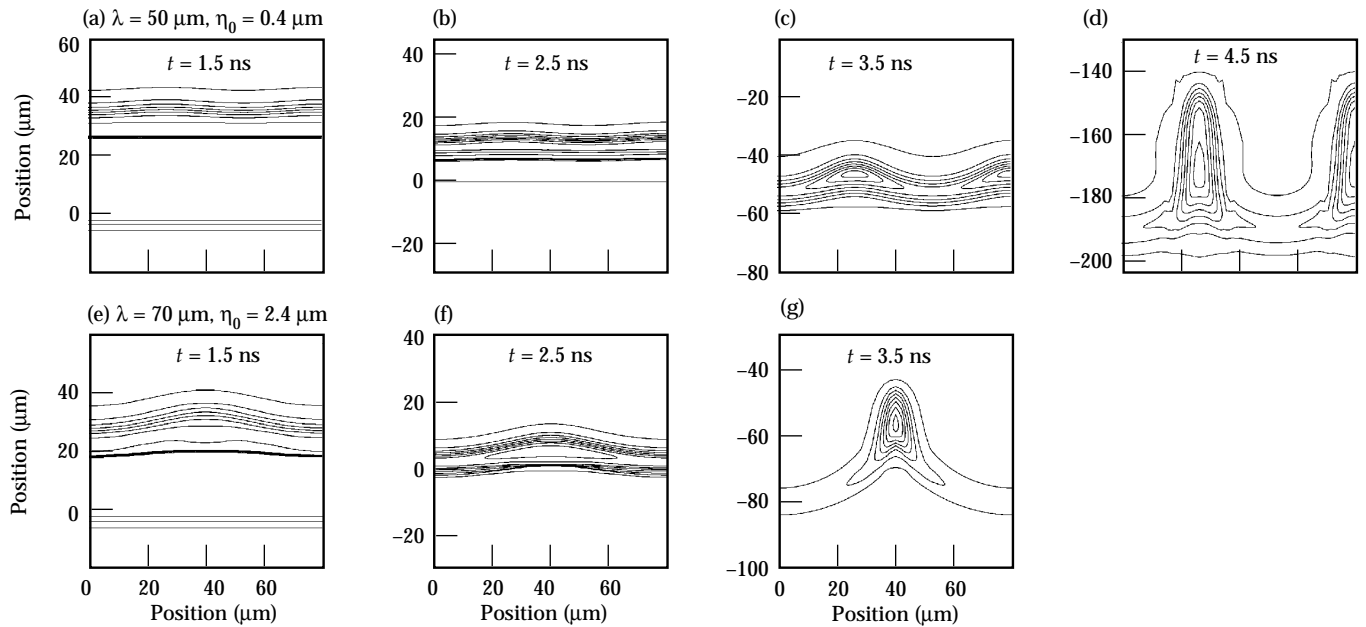
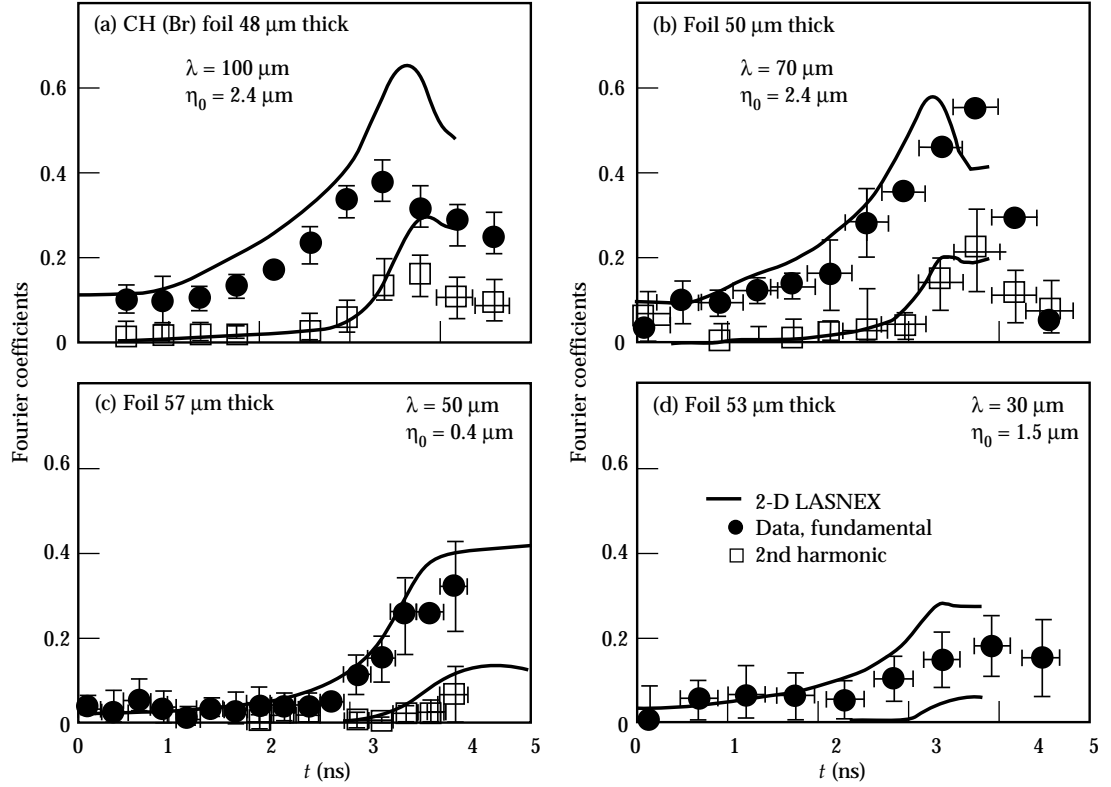


FIGURE 15. Isodensity contour plots from 2-D simulations, in 1-ns steps, for perturbation growth from (a–d) $\lambda = 50 \mu\text{m}$, $\eta_0 = 0.4 \mu\text{m}$ and (e–g) $\lambda = 70 \mu\text{m}$, $\eta_0 = 2.4 \mu\text{m}$, corresponding to the results shown in Figs. 14(c) and 14(b), respectively. The contours correspond to equal density steps and span densities of (a) 0.2177–3.265, (b) 0.4837–7.256, (c) 0.3389–5.084, (d) 0.1548–2.322, (e) 0.2287–3.431, (f) 0.4976–7.464, and (g) 0.5786–8.679 g/cm^3 . (20-03-0894-3227pb02)

This basic behavior can be understood in terms of the simple linear and perturbation theories outlined in Eqs. (2, 3, 5). In the linear regime, RT growth is exponential. For $\eta/\lambda \geq 0.1$, the evolution enters the nonlinear regime, higher harmonics appear, and at third order, the growth in the fundamental mode is reduced. The late-time rollover in the simulations (and presumably in the data), is partially an instrumental artifact, however. Mass is being concentrated in long, narrow spikes in the nonlinear phase, as illustrated in Fig. 15 with isodensity contour plots from the simulations for $\lambda = 50$ and $70 \mu\text{m}$. For example, at $t = 3.5$ ns for $\lambda = 70 \mu\text{m}$ [Fig. 15(g)], 50% of the highest density contours lie within a $10\text{-}\mu\text{m}$ region at the center of the spike, which is difficult to resolve with the $10\text{--}15\text{-}\mu\text{m}$ resolution of the imaging instrument used (see Fig. 4). The observed contrast is therefore decreasing after $t = 3.5$ ns. Notice that there is much less concentration of material in the spike at 3.5 ns for $\lambda = 50 \mu\text{m}$ [Fig. 15(c)]. For this case, spatial resolution does not become an issue until very late ($t \approx 4.5$ ns). For completeness, Fig. 16 shows the simulations before and after convolution with the instrument resolution function. The contrast is greater before inclusion of the MTF, the difference being greatest for the shortest wavelengths.

The simulations systematically predict slightly more growth than is observed (Fig. 14). The seeds of this discrepancy occur early—by 1.5 ns for the $\lambda = 100$ and $70\text{-}\mu\text{m}$ foils, well before the shock has broken out—so the disagreement occurs during the shock transit phase. We consider possible causes for this discrepancy in Fig. 17, using the $\lambda = 70 \mu\text{m}$ experiment as a test case.

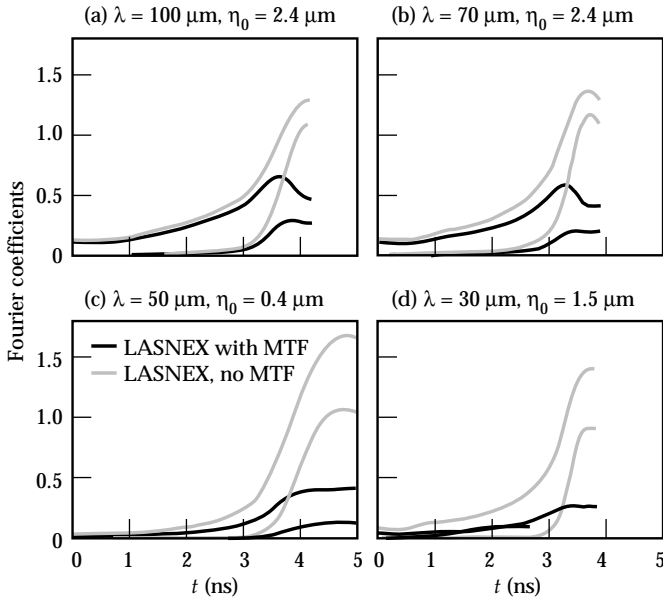


FIGURE 16. Effect of instrument resolution on the results from the simulations. Black curves in (a)–(d), which include the effects of instrumental MTF, are reproduced from Fig. 14. Gray curves represent the simulation results before inclusion of MTF. (20-03-0394-0745pb03)

Possible uncertainties in the drive $T_R(t)$ could arise from uncertainties in the albedo of the Au hohlraum wall early in time and from stagnation of Au plasma on the hohlraum axis late in time. To assess the sensitivity of perturbation growth to uncertainties in the drive, we compare in Fig. 17(a) the results of simulations in which the foot of the drive was 10 eV higher and the peak 10 eV lower than the nominal drive. This variation in the drive produces very little variation in the predicted overall growth for $\lambda = 70 \mu\text{m}$.

Different EOS models can lead to different predicted foil compression, which affects the RM-like growth during shock transit. In Fig. 17(b) we compare the effect of using a tabular EOS library with that of using an in-line QEOS model.⁴⁶ The QEOS model generates a slightly stiffer EOS, which leads to less foil compression and hence to $\sim 15\%$ less perturbation growth.

There is also uncertainty in the exact magnitude of preheat in the drive spectrum early in time. In Fig. 17(c) we assess the sensitivity of perturbation growth to preheat by comparing simulations with a nominal drive spectrum and with a “high preheat” drive, in which the drive spectrum above $h\nu = 1.4$ keV is increased by a factor of 10 for the first 2 ns, while keeping the total

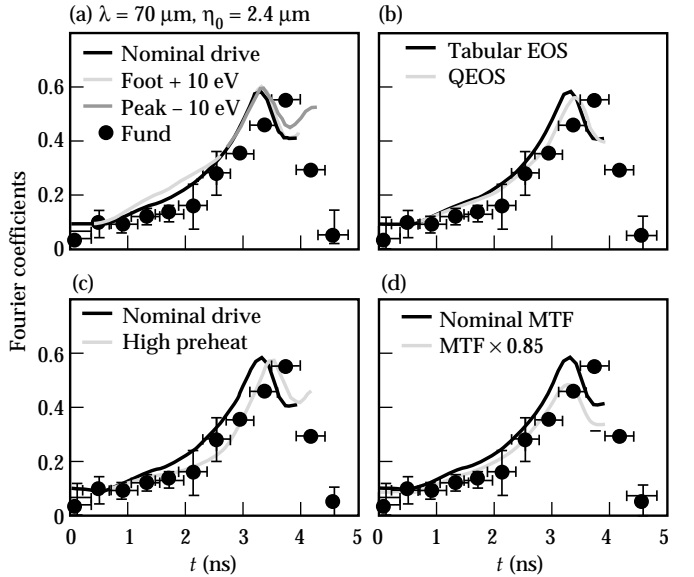


FIGURE 17. Sensitivity of perturbation growth for $\lambda = 70 \mu\text{m}$, $\eta_0 = 2.4 \mu\text{m}$ to (a) drive, (b) EOS, (c) preheat, and (d) MTF. Data and black curves are reproduced from Fig. 14(b). (a) The light gray curve corresponds to a simulation in which the radiation temperature in the foot of the drive was increased by 10 eV; the dark gray curve represents a simulation in which the peak of the drive was reduced by 10 eV. (b) The nominal simulation (black) uses a tabular EOS library. The gray curve uses an in-line model called QEOS, which results in a slightly “stiffer” EOS. (c) The gray curve corresponds to a simulation in which the preheat in the drive was artificially increased: during the first 2 ns (the foot), the drive for $h\nu \geq 1.4$ keV was increased by a factor of 10, and the drive for $h\nu < 1.4$ keV was decreased to maintain the same total energy. (d) The gray curve corresponds to post-processing the simulation with a resolution function artificially degraded to give a 15% lower MTF. (20-03-0894-2839pb03)

drive power constant. Enhancement of the preheat significantly reduces perturbation growth.

We also illustrate the sensitivity of observed growth to uncertainties in the MTF. Decreasing the MTF by 15%, the maximum reduction consistent with the data shown in Fig. 4(a), decreases the predicted growth by 15%, as shown in Fig. 17(d).

To summarize, the simulations slightly but systematically overpredict perturbation growth during the shock transit phase. A possible cause is higher preheat in the foot of the drive, but a combination of stiffer EOS and degraded MTF may also be involved.

We have also done single-mode 2-D experiments aimed at measuring large RT growth factors.¹⁴ These experiments differed from those described above only in the use of fluorosilicone ($\text{SiOC}_4\text{H}_7\text{F}_3$, or “FS”) as the foil material. We used FS because its admixture of opacities shields the foil from x-ray preheat, keeping the foil on a lower adiabat. The density gradient at the ablation front is therefore steeper, and the ablation velocity is lower, leading to higher RT growth factors.

We did these experiments in an amplitude-scaling series, starting with large amplitude to see the initial contrast easily. In this case, however, the RT evolution quickly enters the nonlinear regime, higher harmonics are formed, the perturbation takes on the classic bubble-and-spike shape, and the growth slows sharply, ultimately changing from exponential to linear. We then shot an intermediate-amplitude target, which entered the nonlinear regime only towards the end of the acceleration. Finally, to maximize the observed growth, we used a very-small-amplitude perturbation, so that the foil remained in the linear regime throughout the acceleration. Figure 18 shows the results. For the smallest amplitude perturbation, a growth factor of 75 was observed in the fundamental mode. The peak-to-valley amplitude grew by a factor of 80 (that is, 4.4 e -foldings of growth), in agreement with the simulations.

To better illustrate the differences between the evolution of these three targets, we use the simulations to show in Fig. 19 the actual shape of the perturbations at peak growth. The large- η_0 foil [Fig. 19(a)] shows the classic bubble-and-spike shape of the nonlinear RT

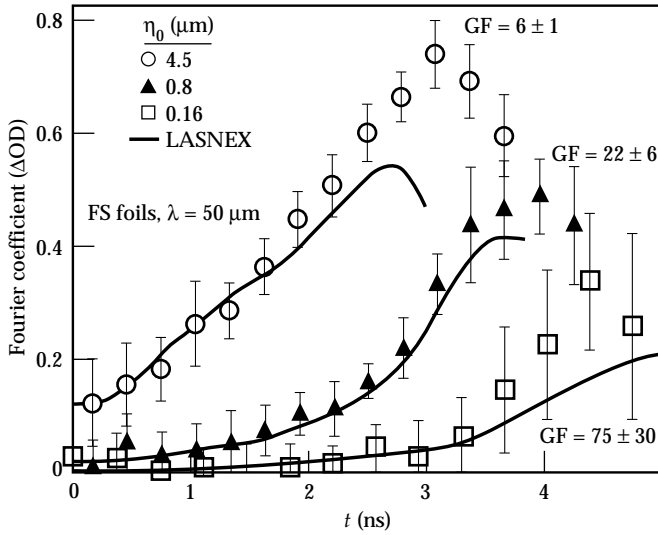


FIGURE 18. Amplitude (η_0) scaling results for three fluorosilicone (FS) foils. Perturbations were $\lambda = 50 \mu\text{m}$, $\eta_0 = 0.16, 0.8$, and $4.5 \mu\text{m}$; the smallest- η_0 perturbation yielded the highest growth factor ($G = 75$). (20-03-1293-4395pb01)

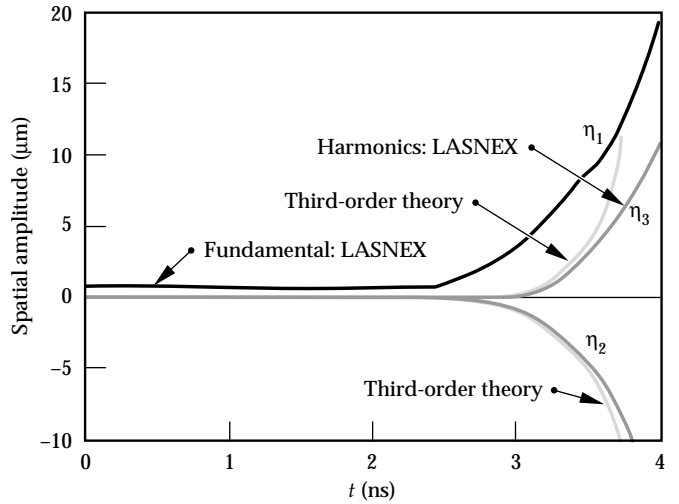


FIGURE 20. LASNEX simulations of the RT evolution for the intermediate- η_0 foil (from Fig. 18), and corresponding results from third-order perturbation theory. (20-03-0895-2046pb01)

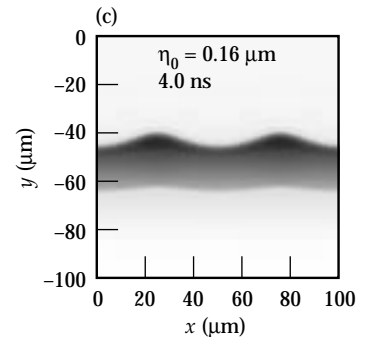
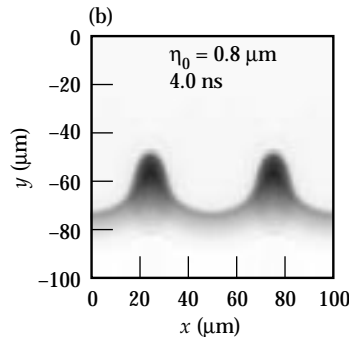
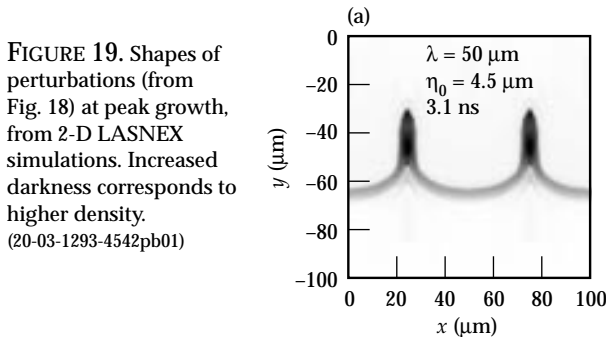


FIGURE 19. Shapes of perturbations (from Fig. 18) at peak growth, from 2-D LASNEX simulations. Increased darkness corresponds to higher density. (20-03-1293-4542pb01)

regime; the small- η_0 foil [Fig. 19(c)] still looks largely sinusoidal, indicating linear RT evolution; the intermediate- η_0 foil [Fig. 19(b)] is midway in between.

The transition to the nonlinear regime can be illustrated qualitatively with third-order perturbation theory.^{14,23} We compare the results from the LASNEX simulation for the intermediate- η_0 foil ($\eta_0 = 0.8 \mu\text{m}$) with those obtained from perturbation theory [Eq. (5)]. Amplitudes in areal density ρR are converted to spatial amplitude by dividing by a characteristic density. Figure 20 shows the results. Third-order perturbation theory predicts the entry into the nonlinear regime very well.

The quantity of most interest in RT instability studies is the growth rate γ in Eq. (2), which is often parametrized as in Eq. (3) in terms of foil acceleration g , density ρ , and density gradient scalelength L . Unfortunately, because of the nature of our low-adiabat drive, the foil g , ρ , and L are not constant, as shown in Figs. 11 and 12. Hence, our RT growth cannot be characterized in terms of a single value of γ over the full duration of the foil acceleration. Nevertheless, from linear-regime simulations for $\lambda = 50 \mu\text{m}$ [Figs. 21(b), 21(c)], we show the dispersion curves in Fig. 21(d) for CH(Br) and FS, using parameters characteristic of the foils at $t = 3.0 \text{ ns}$. Even though the exact quantitative form of Eq. (3) for indirect drive is not settled, the

equation appears qualitatively to describe the effect of stabilization at the ablation front. This has recently been demonstrated conclusively by comparing RT growth at the ablation front with that at an embedded interface, away from the ablation front, for this same drive and ablator material. At the ablation front, no growth was observed for wavelengths shorter than $30 \mu\text{m}$, whereas at the embedded interface, strong growth down to wavelengths as short as $10 \mu\text{m}$ was observed.⁴⁷

Earlier experiments were done with a 1-ns drive pulse shape, using FS and CH foils.¹³ Figure 22 shows the results. This drive puts the foils on a much higher adiabat; the duration of the acceleration was short, and the growth was predominantly due to the rippled shock dynamics. Growth factors were $G \approx 2.5$ and $G = 1.5$ for the FS and CH foils, respectively.

All of our single-mode 2-D experiments can be qualitatively understood by the density profiles in Fig. 23, where we have carried out 1-D LASNEX simulations with the shaped drive, changing only the foil material. The FS foil remains on the lowest adiabat, has the steepest density gradient at the ablation front, and (as we saw above) exhibits the largest RT growth factors. The CH foil is at the opposite extreme. With no opacity shield against the hard x rays in the drive, the CH foil jumps to a very high adiabat, the density gradient at

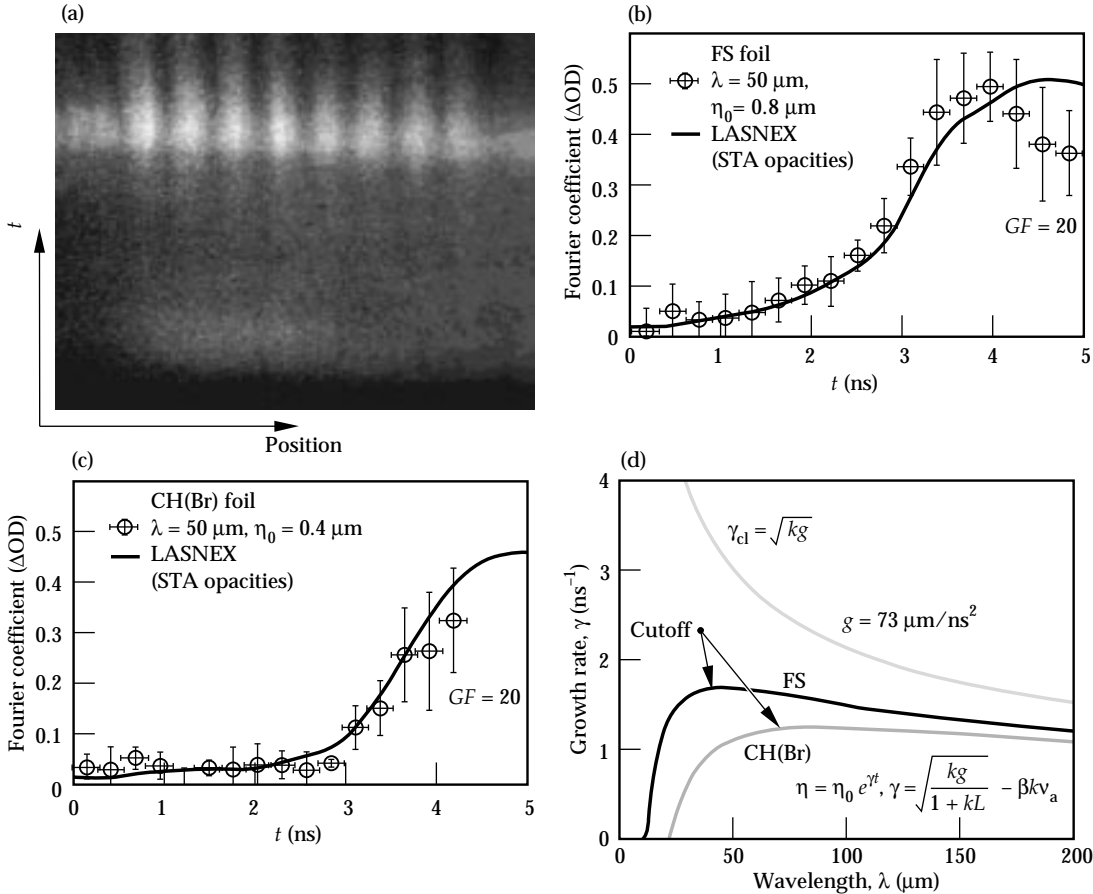


FIGURE 21. Results for intermediate- η_0 foil (from Fig. 18): (a) raw data, (b) Fourier coefficient of fundamental mode vs time. (c) As in (b), but for a CH(Br) foil (from Fig. 14c). (d) Dispersion curve for FS and CH(Br) with $\beta = 2.5$: for FS, $L = 1.6 \mu\text{m}$, $v_a = 3.2 \mu\text{m/ns}$; for CH(Br), $L = 4.0 \mu\text{m}$, $v_a = 3.9 \mu\text{m/ns}$. (20-03-1293-4398pb01)

the ablation front has only a very gentle slope, the ablation velocity is very high, the RT growth is practically zero, and the foil burns through quickly. The CH(Br) foil falls between these two extremes.

Two-Mode Experiments

We next turn to the two-mode experiments.^{37,48} Figure 24(a) shows the two-mode perturbations we investigated; the upper side of each curve corresponds to the foil. Figure 24(a) shows a large-amplitude two-mode perturbation given by $\lambda_2 = 75 \mu\text{m}$ and $\lambda_3 = 50 \mu\text{m}$, with $\eta_2 = \eta_3 = 2 \mu\text{m}$.

Characterization of the initial perturbations is critical for proper interpretation of the RT growth. The initial perturbations are characterized by three independent techniques—interferometry, contact profilometry, and x-ray radiography—and are accurate to 10% or better. Figure 25 shows examples of characterization by profilometry and radiography for the two-mode foils (and for the eight-mode foils of the next section, “Eight-Mode Experiments”). The agreement between the two techniques is very good except at the shortest wavelengths ($\lambda \leq 25 \mu\text{m}$) because of the finite resolution of our radiography setup. We use the η_n from contact profilometry as the most accurate initial amplitudes.

Figure 26 shows the results for the large-amplitude two-mode foil shown in Fig. 24(a). Figure 26(a) shows the raw image, and Fig. 26(b) shows a profile of $\ln E$ at 2.7 ns aligned relative to the mold, showing how the phase of the data is established. Figure 26(c) illustrates the analysis technique with a profile of $\ln E$ at 3.3 ns. To remove the long-range structure arising from the backlighter, we fit a low-order polynomial to the profile of $\ln E$, shown by the gray curve. The lower solid curve in

Fig. 26(c) shows the $\ln E$ profile after having subtracted the fit to the backlighter structure. The vertical dotted lines represent the boundaries for the Fourier analysis. The histogram in Fig. 26(d) shows the real component of the Fourier transform of $\ln E$ at 3.3 ns. Because of the cosine symmetry of the perturbation, the imaginary component (not shown) is identically zero except for random noise.

The Fourier modes are enumerated as harmonics of the longest repeating pattern ($150 \mu\text{m}$). Hence, the two pre-existing modes are k_2 ($\lambda = 75 \mu\text{m}$) and k_3 ($\lambda = 50 \mu\text{m}$). Because the initial amplitudes are large, the perturbation

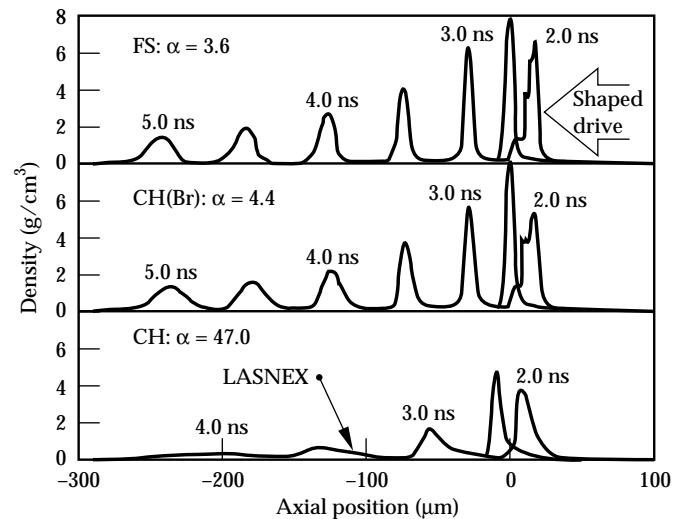
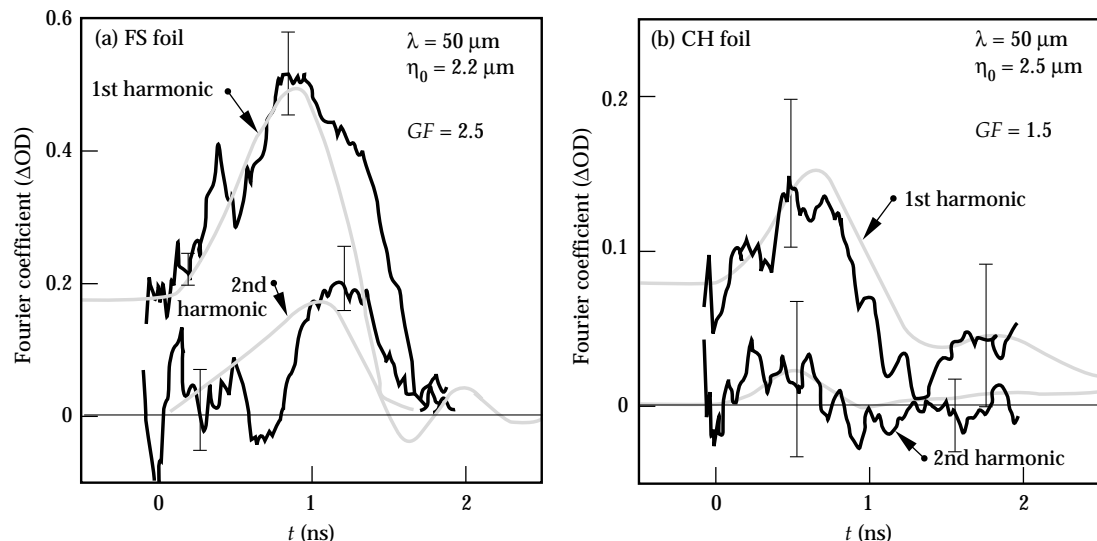


FIGURE 23. Density profiles from 1-D LASNEX simulations for FS, CH(Br), and CH, assuming the same low-adiabat drive for each. (20-03-1293-4401pb01)

FIGURE 22. Results from the 1-ns square drive pulse shape for (a) FS and (b) CH foils. For this high-adiabat drive, the growth factors were $G < 3$. (20-03-1293-4400pb02)



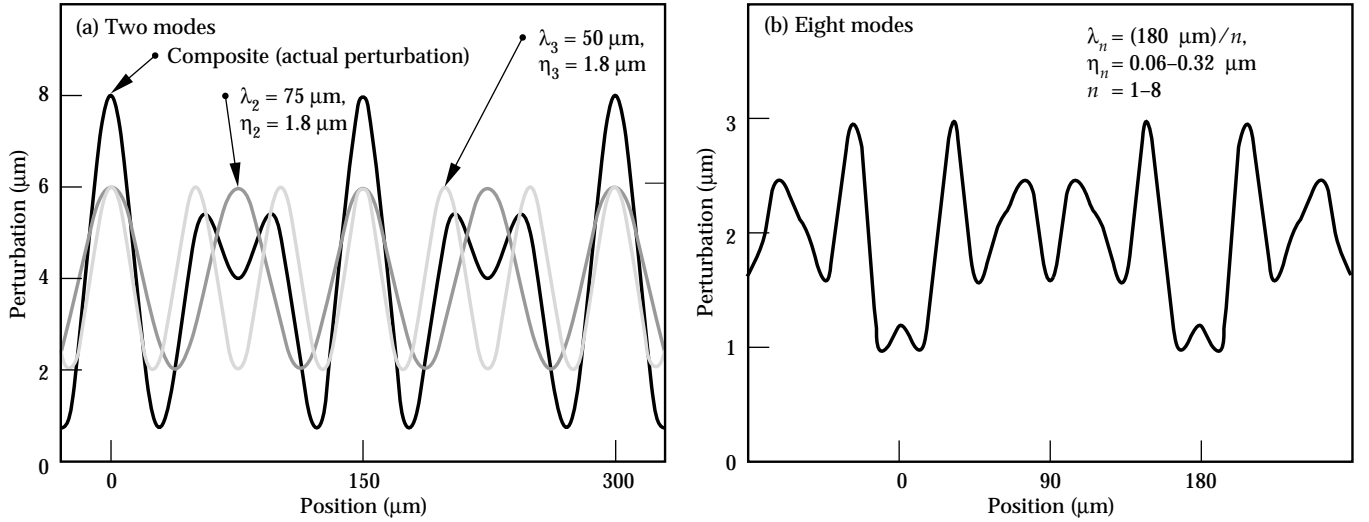


FIGURE 24. Multimode perturbation patterns investigated. (a) Two-mode perturbation: curves correspond to $\lambda_2 = 75 \mu\text{m}$, $\eta_2 = 1.8 \mu\text{m}$ and $\lambda_3 = 50 \mu\text{m}$, $\eta_3 = 1.8 \mu\text{m}$. Their superposition represents the actual perturbation. The foil corresponds to the upper side of the curve. (b) Eight-mode perturbation corresponds to the sum of wavelengths $\lambda_n = (180 \mu\text{m})/n$, $n = 1-8$; Table 1 gives corresponding amplitudes. (20-03-0394-0741pb03)

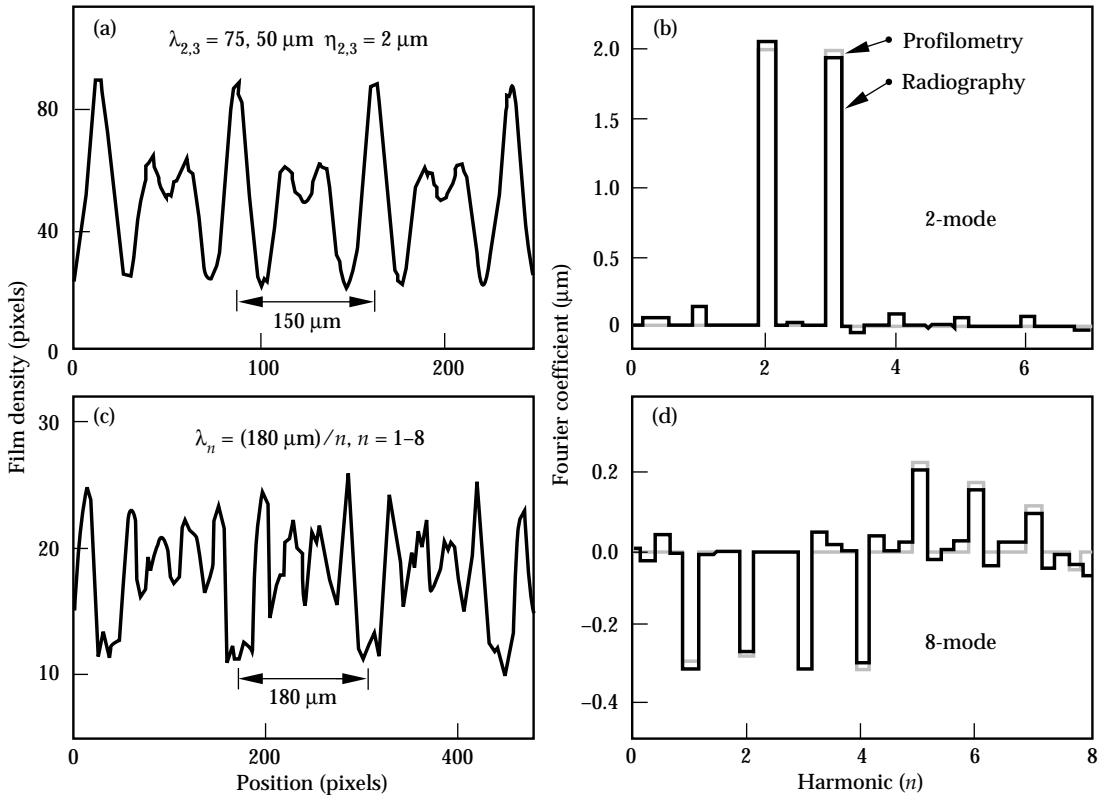


FIGURE 25. Multimode perturbations characterized by contact profilometry and radiography. (a) Lineout from the 2-D radiograph of the large-amplitude two-mode perturbation shown in Fig. 24(a). The contact radiograph corresponds to a 2-hr exposure on Kodak high-resolution glass plate film using a Mo anode at an electron accelerating voltage of 5 kV and a 1- μm Ag filter. (A film density of 1024 pixels corresponds to an optical depth of 5.115.) The film response is removed using a simultaneous exposure across a Be step wedge covering the same range in optical depth. (b) The black histogram is the real component of the Fourier transform of the curve shown in (a). The gray histogram represents the Fourier transform of the contact profilometer trace (not shown), and is essentially identical with the radiography result. (c) Same as (a) except for the eight-mode perturbation shown in Fig. 24(b). (d) Same as (b) except for the eight-mode perturbation. (20-03-0394-0742pb03)

quickly evolves into the nonlinear regime with the appearance at 3.3 ns of the second harmonic of k_2 , namely, $2k_2$. We also observe very distinct $k_1 = k_3 - k_2$ and $k_5 = k_3 + k_2$ coupled modes corresponding to $\lambda = 150$ and $30 \mu\text{m}$, respectively. Notably absent is the second harmonic of k_3 , namely, $2k_3$. This is because $3k_2$, the third harmonic of k_2 , has the same magnitude as $2k_3$ but the opposite sign, leading to a cancellation.

The results shown in Fig. 26(d) are rather insensitive to the exact functional form used in fitting the background. The smooth gray curve shown in Fig. 26(c) corresponds to a fifth-order polynomial fit. If we had chosen a second-order polynomial to fit the background, the k_1 term would have been 5% larger, and the other modes would have changed by $\sim 1\%$. With no background subtraction at all, the k_1 mode would have been only 20% different, and the other modes would have varied by $\sim 5\%$ or less. This is illustrated by showing the Fourier composition of the background itself. The gray curve in Fig. 26(d) corresponds to the Fourier transform of the gray curve in Fig. 26(c). Thus there is little sensitivity to the exact details of how we treat the backlighter background subtraction.

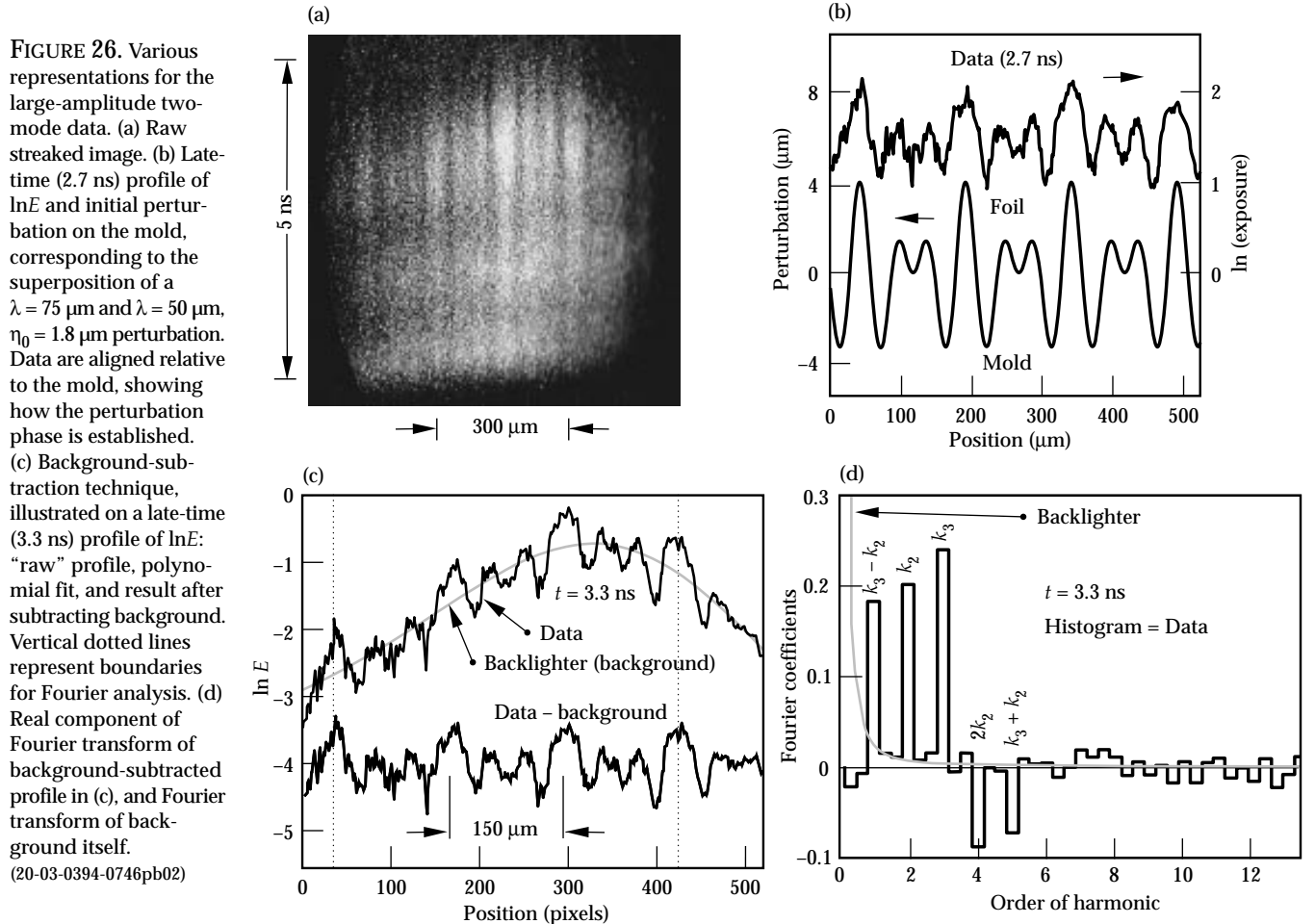
It is instructive to view these nonlinear mode coupling effects within the context of perturbation theory.²⁶ We

consider here only a qualitative application for the coupling from two pre-existing modes k_2 and k_3 using Eq. (8) from the Introduction, namely,

$$\eta_{k_i \pm k_j} \approx \mp \frac{1}{2} (k_i \pm k_j) \eta_{k_i}^L \eta_{k_j}^L; \quad (8)$$

where $\eta_{k_n}^L$ represents the spatial amplitude of mode k_n had the growth been entirely in the linear regime. Notice that $\eta_{k_3 - k_2}$ has the same sign as the product $\eta_{k_2}^L \eta_{k_3}^L$, whereas $\eta_{k_3 + k_2}$ has the opposite sign, in agreement with the experimental observation shown in Fig. 26(d). If the boundaries of the Fourier transform are shifted by $75 \mu\text{m}$ (that is, by half of the fundamental $n = 1$ period), the k_2 and k_3 modes have opposite signs (not shown). The $k_3 - k_2$ mode is then negative, and the $k_3 + k_2$ mode is positive, again in agreement with Eq. (8). Qualitatively at least, the observation of the $k_3 \pm k_2$ coupled terms can be understood from second-order perturbation theory. The modes are too large already by shock breakout to apply second-order theory quantitatively, however.

Figure 27 shows the full time dependence of the two-mode data shown in Fig. 26. The plotting symbols represent the data, which again correspond to the real



component of the Fourier transform of $\ln E$. Because of symmetry, the imaginary component of the Fourier transform should be zero, and we take its value as a measure of the error for each point. The $k_3 \pm k_2$ coupled terms are not observed until after about $t = 2.5$ ns, after the perturbation has entered the nonlinear regime. The black curves in Fig. 27 are the corresponding results from 2-D LASNEX simulations, after convolution of the simulated image exposure with the instrumental spatial resolution function [Eq. (11)]. The gray curves in Fig. 27(a) correspond to simulations of the evolution of each mode had it been the only mode initially present. The departure of the black curves from the gray curves for $t \geq 3$ ns coincides with the growth of the coupled terms, as shown in Fig. 27(b). The Fourier composition of the perturbation is redistributed into a broader spectrum because of the $k_3 \pm k_2$ mode coupling. This corresponds in physical space to a change of shape: mode coupling makes the bubbles broader and flatter and the spikes narrower. This is illustrated explicitly in the next section.

Eight-Mode Experiments

Figure 24(b) shows a small-amplitude eight-mode perturbation given by $\lambda_n = (180 \mu\text{m})/n$. The individual amplitudes η_n (given in Table 1) are about a factor of 10 smaller than those for the two-mode foil. Figure 28(a) shows the raw image of the experimental shot, and Fig. 28(b) gives a late-time profile of $\ln E$ aligned relative to the mold, showing how the phase of the data is established.^{37,48} The vertical dashed lines indicate the boundaries for the Fourier analysis. The black histograms in Figs. 28(c) and 28(d) show the real component of the Fourier transform at an early time (3.2 ns) and at late time (4.4 ns). Because of the cosine symmetry, the imaginary component (shown by the gray histograms)

oscillates around the baseline as random background and serves as an estimate of the error. Early in time in the linear regime [Fig. 28(c)], only the pre-existing modes grow, in accordance with their initial amplitudes and growth rates. The k_3 mode ($\lambda = 60 \mu\text{m}$) dominates. Late in time [Fig. 28(d)], the perturbation has entered the nonlinear regime and the modes no longer grow independently. The k_3 mode no longer dominates, its magnitude having been reduced by $k_3 - k_2$ mode coupling to drive up the k_1 mode. This causes the k_1 term to reverse phase; the initial sign of the k_1 mode was negative, as given in Table 1.

Figure 29 shows the full time evolution of the eight-mode data. The plotting symbols correspond to the real component of the Fourier transform of the data, and the error bars correspond to the imaginary component. The black curves represent the eight-mode LASNEX simulation after convolving $\ln E$ with the spatial resolution function [Eq. (11)]; the qualitative agreement with the data is good. The light gray curves represent the single-mode simulations, in which it is assumed that each mode existed alone. As a result of mode coupling, modes k_2 through k_5 grow less than they would have alone. Growth reduction is least for mode k_4 , which has the largest amplitude at the time of saturation. The presence of multiple modes causes nonlinearity to occur earlier than if the modes had existed alone.

Modes k_1 , k_6 , and k_7 reverse phase and grow with the opposite sign. These modes show most prominently the effects of coupling from the dominant modes, k_2 , k_3 , and k_4 . The dark gray curves show the amplitudes predicted for these modes from second-order theory, described in more detail below. The phase reversal for mode k_1 , for example, can be understood from Eq. (8) and considering only the dominant modes k_2 , k_3 , and k_4 . Both the $k_3 - k_2$ and $k_4 - k_3$ coupled terms are positive, tending to cause a phase reversal in the growth of

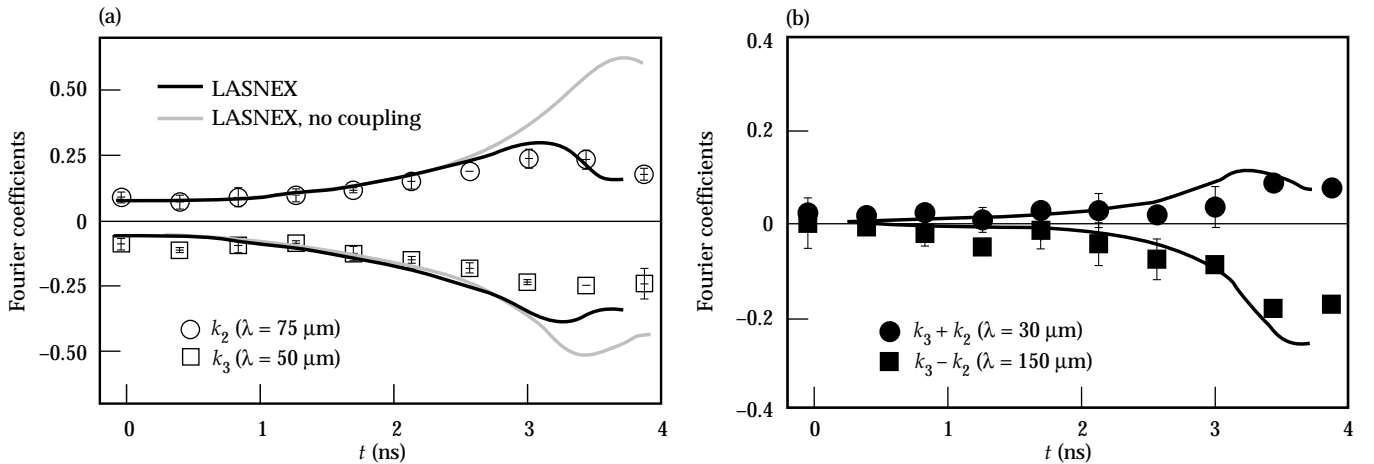


FIGURE 27. Full time dependence for two-mode data of Fig. 26. (a) Results for the $\lambda = 75 \mu\text{m}$ component of the pre-existing perturbation and for k_3 (the $\lambda = 50 \mu\text{m}$ component). (b) The $k_3 + k_2$, $\lambda = 30 \mu\text{m}$ and $k_3 - k_2$, $\lambda = 150 \mu\text{m}$ coupled terms and corresponding 2-D LASNEX two-mode and single-mode results. (20-03-0394-0747pb03)

the k_1 mode (which was initially negative), as observed. Similarly, the phase reversals of modes k_6 and k_7 can also be understood from Eq. (8), considering $k_i + k_j$ coupling from the dominant modes k_2 , k_3 , and k_4 . Figure 29(d) also shows (dashed curve) the result for mode k_4 of an eight-mode simulation with enhanced preheat in the drive (factor of 10 increase in drive spectrum for $h\nu > 1.4$ keV and $t < 2$ ns, as discussed in the earlier section “Single-Mode Experiments”). As in Fig. 17(c), the enhanced preheat reduces the perturbation growth considerably, bringing the simulation into good agreement with the data. This is true for all eight modes, although we show only the enhanced-preheat result for mode k_4 .

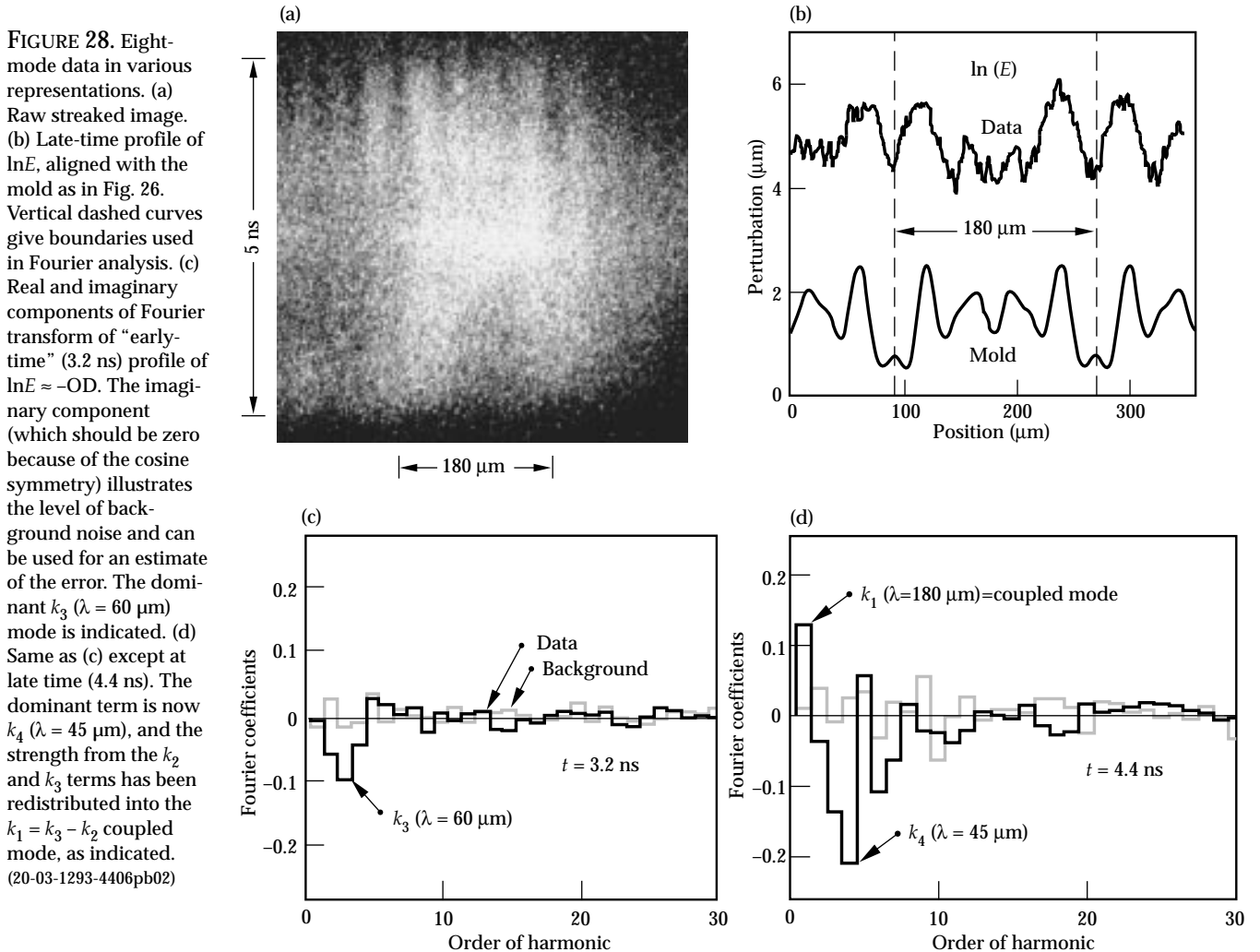
The second-order perturbation model can be quantitatively applied to the eight-mode experiment^{26,37,48,49} using Eq. (A3) from the final section “Amplitude of Coupled Modes,”

$$\eta_k \approx \eta_k^L + \frac{1}{2}k \left(\sum_{k'} \eta_{k'}^L \eta_{k+k'}^L - \frac{1}{2} \sum_{k' < k} \eta_{k'}^L \eta_{k-k'}^L \right), \quad (\text{A3})$$

by summing over the products of all pairs of modes whose sum or difference equals the k of interest. The η_{k_n} represent spatial amplitudes, which we define from the LASNEX simulations by dividing the modulations in areal density by the foil peak density, that is,

$$\eta \text{ (}\mu\text{m)} \approx \frac{\delta \int \rho dz}{\rho_{\text{max}}}. \quad (14)$$

We apply this model to our experiment as follows. For each λ_n in the eight-mode foil, 2-D LASNEX simulations are run for perturbations of very small initial amplitude, ensuring that the RT evolution remains in the linear regime. The $\eta_{k_n}^L(t)$ are then obtained by scaling by the ratio of actual to the assumed initial amplitude. This technique of generating the $\eta_{k_n}^L(t)$ automatically includes the effects of the time-dependent acceleration, compression, density gradient, and ablative stabilization. The dark gray curves in Figs. 29(a), 29(f), and 29(g) show the results from this perturbation analysis for $t \leq 3.7$ ns. After this time, the central assumption of



the model (dominant modes not affected by the coupling terms) is violated and the model is no longer applicable. In each case, the phase reversals are well described by second-order perturbation theory.

At late times ($t \geq 4$ ns), the saturation of modes k_2 and k_3 results from the redistribution of the Fourier components because of mode coupling. In physical space, this corresponds to a change in shape, as illustrated in Fig. 30 for the two-mode and eight-mode perturbations. The black curves correspond to profiles of $\ln E$ taken from the LASNEX simulations before inclusion of the instrument spatial resolution function. The gray curves represent the sum of the results from the single-mode simulations. Comparing the gray and black curves, we see that the shapes of the perturbations with and without mode coupling differ. With mode coupling, the bubbles are broader and flatter and the spikes are narrower. This shape effect has been observed in other simulations,²⁹ but to our knowledge this is the first experimental observation of the effect in ablatively accelerated foils.

The results from our eight-mode experiment can also be compared with results from a saturation model developed for a full continuum of initial modes.³² The basic premise of this model is that a perturbation corresponding to a full continuum of modes saturates when the product $k_{\text{char}}\eta_{\text{char}}$ is no longer small, that is, when

$$\eta_{\text{char}} = \varepsilon_1 \lambda_{\text{char}} = \frac{2\pi\varepsilon_1}{k_{\text{char}}}, \quad (15)$$

where η_{char} and λ_{char} are a characteristic spatial amplitude and wavelength and ε_1 is some number less than

unity. But η_{char} can be approximated as the quadrature sum of individual modes within a band Δk centered around $k_{\text{char}} = 2\pi/\lambda_{\text{char}}$, namely,

$$\eta_{\text{char}} = \left(\sum_{\Delta k} \eta_k^2 \right)^{1/2} \approx \left(\Delta k \frac{L}{2\pi} S_k^2 \right)^{1/2} \approx \left(\varepsilon_2 k \frac{L}{2\pi} S_k^2 \right)^{1/2}, \quad (16)$$

where $\Delta k = \varepsilon_2 k$ for some $\varepsilon_2 < 1$, L is the system size, $L/2\pi$ is the 2-D density of Fourier states, and S_k is a

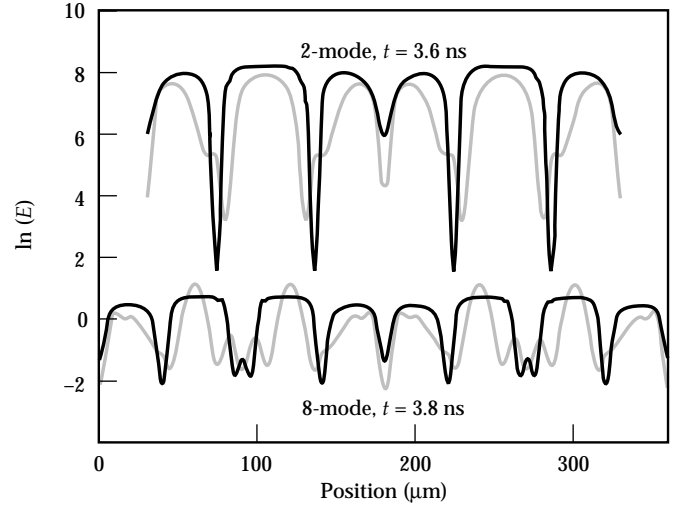


FIGURE 30. Effect of mode coupling on perturbation shape. The upper black curve represents the two-mode simulation at 3.6 ns, and the upper gray curve corresponds to the sum of the simulations for the two individual modes run alone. The lower curves are the same only for the eight-mode perturbation at 3.8 ns. (20-03-0194-0106pb02)

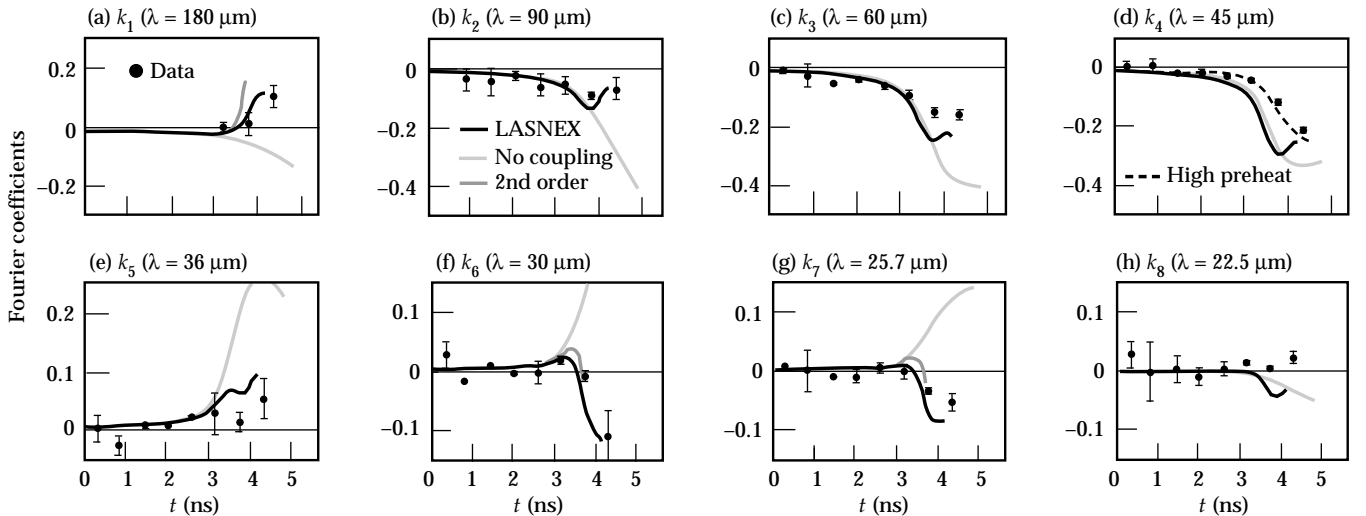


FIGURE 29. Full time dependence for data shown in Fig. 28. (a)–(h) Growth of modes $\lambda_{n_i} = (180 \mu\text{m})/n$, $n = 1$ –8, vs time. Solid circles represent data; black curves represent corresponding 2-D LASNEX simulations. Light gray curves represent simulations under the assumption that each individual mode existed alone, and the dark gray curves for modes k_1 , k_6 , and k_7 correspond to the results of a calculation using weakly nonlinear, second-order perturbation theory. The dashed line for mode k_4 corresponds to a simulation with assumed enhanced preheat in the foot of the drive. (20-03-0394-0749pb03)

typical spatial amplitude of an *individual* mode within Δk . Combining Eqs. (15) and (16) gives

$$S_k = \frac{v_{2D}}{L^{1/2} k^{3/2}}, \quad (\text{in 2-D}), \quad (17a)$$

$$S_k = \frac{v_{3D}}{L k^2} \quad (\text{in 3-D}), \quad (17b)$$

where ε_1 and ε_2 have been combined into a single parameter v (set in Ref. 32 for the 2-D case to $v_{2D} = 1.14$), and L represents here the longest wavelength in the periodic perturbation, $L = 180 \mu\text{m}$. The result for 3-D given in Eq. (17b) is derived the same way, but with $\varepsilon_2 k$ replaced by $(\varepsilon_2 k)^2$, and the density of states factor becomes $(L/2\pi)^2$. The normalization $v_{2D} = 1.14$ was arrived at by comparison with the classical (incompressible) fluid RT experiments of Read and Youngs.⁵⁰ The above saturation results, namely Eq. (17a) and (17b), can be derived more elegantly as follows. A multimode perturbation in a localized region of space can be thought of as a wavepacket. Over a small but finite spectral range, this wavepacket cannot be distinguished over short distances from a single-mode at wave vector k . We expect RT saturation to occur at roughly the same amplitude in both cases (wavepacket vs single-mode), which means that amplitudes at saturation of the individual components of the wavepacket will be less than the amplitude of the single mode. Based on the criterion of Layzer for a single mode,²⁵ saturation is expected to occur when the spacial amplitude η reaches $\sim(0.6/k)$. In the multimode case, an additional factor of λ/L enters to account for the number of similar modes about k that can contribute to the saturation of mode k . Hence $S_k \approx \lambda/kL = 2\pi/k^2 L$, as given by Eq. (17b). We apply this saturation model, namely Eq. (17a), to our eight-mode experiment by calculating with LASNEX the growth of each mode k_n in the linear regime until its spatial amplitude defined by Eq. (14) exceeds the S_{k_n} given by Eq. (17). At this time we make a smooth transition to bubble growth that is linear in time, corresponding to a terminal bubble velocity equal to the velocity at saturation. This transition to saturated growth is accomplished with the logarithmic construction

$$\eta_k(t) = S_k \left\{ 1 + \ln \left[\eta_k^L(t) / S_k \right] \right\}, \quad (18)$$

where $\eta_k^L(t)$ represents the spatial amplitude had the growth remained in the linear regime. The modes are added in quadrature to produce the predicted root-mean-square (rms) bubble amplitude. We compare this with the rms bubble amplitude from the LASNEX eight-mode simulation. Bubbles are defined in terms of foil areal density $\int \rho dz$ (that is, the foil ρr) by considering only those perturbations leading to $\rho r < (\rho r)_{av}$. Figure 31 shows the result for the nominal $v_{2D} = 1.14$ and for values of v_{2D} a factor of 2 higher and lower

than 1.14. The result corresponding to $v_{2D} = 0.57$ agrees best with the LASNEX eight-mode simulation. This is only a crude test of the model for ablatively accelerated foils, because the density of Fourier modes is low. Future work will involve 3-D experiments with a near continuum of modes and larger growth factors as a better test of this saturation model.

3-D Single-Mode Experiments

The nonlinear RT growth of a perturbation depends upon its shape. Perturbations of the same magnitude wavenumber $k = (k_x^2 + k_y^2)^{1/2}$ can have different shape and can therefore evolve differently in the nonlinear regime while having the same linear-regime RT growth rate. In this section we examine how the 3-D shape affects the growth of single-mode perturbations on planar foils.⁵¹ The CH(Br) foils were made using a new laser ablation technique to make molds in Kapton or Mylar substrates.⁵² We prepared perturbed foils all with the same magnitude wave vector $k = (k_x^2 + k_y^2)^{1/2}$ and nominally the same amplitude. The “2-D” foil (1-D wave vector $k = k_x$) was a simple $\lambda = 50 \mu\text{m}$ sinusoid with initial amplitude $\eta_0 = 2.5 \mu\text{m}$. One of the “3-D” foils [2-D wave vector $k = (k_x, k_y)$] corresponded to a “stretched” $k_x = 3k_y$ perturbation, and the other was a square $k_x = k_y$ mode. The three foils were characterized using contact radiography [Fig. 32(a)–32(c)] and contact profilometry. The radiographs were converted to spatial amplitudes using a CH(Br) step wedge. Figure 32(d)–32(f) show corresponding images from Nova shots at 4.3 ns, which is near peak growth. The gated x-ray pinhole camera for these images was run at 8× magnification

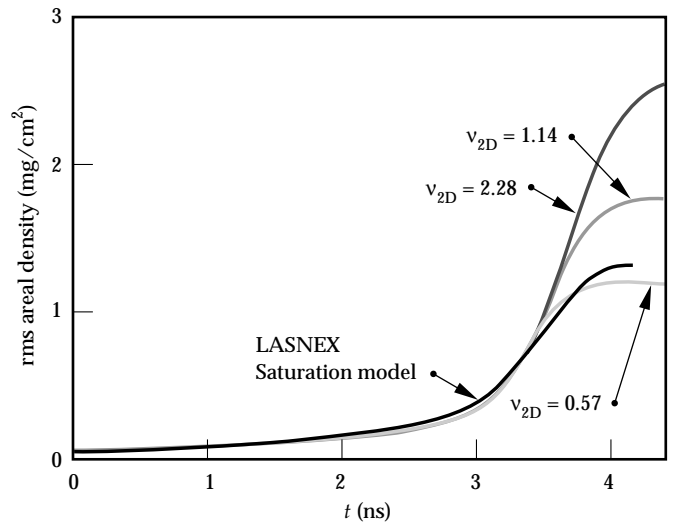


FIGURE 31. Results of eight-mode LASNEX simulation and corresponding results from multimode saturation theory. Black curve corresponds to the rms perturbation in areal density $\Delta \int \rho dz$ from the eight-mode simulation, where we consider only the bubble amplitude. Other curves correspond to results of the saturation model for normalizations [Eq. (17a)] of $v_{2D} = 2.28, 1.14$, and 0.57 . (20-03-0194-0131pb02)

with 10- μm pinholes and 150- μm Be filtering. The backlighter was Sc at 4.3 keV.

Each image from the Nova shots [Fig. 32(d)–32(f)] is converted to $\ln E \propto -OD = -\int \rho \kappa dz$. Hence, modulations in $\ln E$ correspond to modulations in foil areal density. To visualize the 3-D RT evolution better, we focus momentarily on the $k_x = k_y$ mode. Figure 33(a) gives a 3-D surface perspective of the data shown in Fig. 32(f). Figure 33(b) shows the corresponding simulation with the new 3-D radiation–hydrodynamics code HYDRA.⁵³ The height of these surfaces is proportional to $-(\text{areal density})$, and crudely speaking, represents the boundary

between the hot, low-density ablated plasma and the dense pusher material ahead of it.

In the reference frame of the accelerating ablation front, one would see a broad, hot bubble of ablated plasma rising up through the pusher and spikes of dense pusher fluid falling essentially freely through the ablated plasma. This canonical shape of the 3-D RT instability can be understood from a simple buoyancy-vs-drag equation,^{54,55}

$$\rho_1 V \frac{\partial u}{\partial t} = (\rho_1 - \rho_2) V g - c_D \rho_1 u^2 S, \quad (19)$$

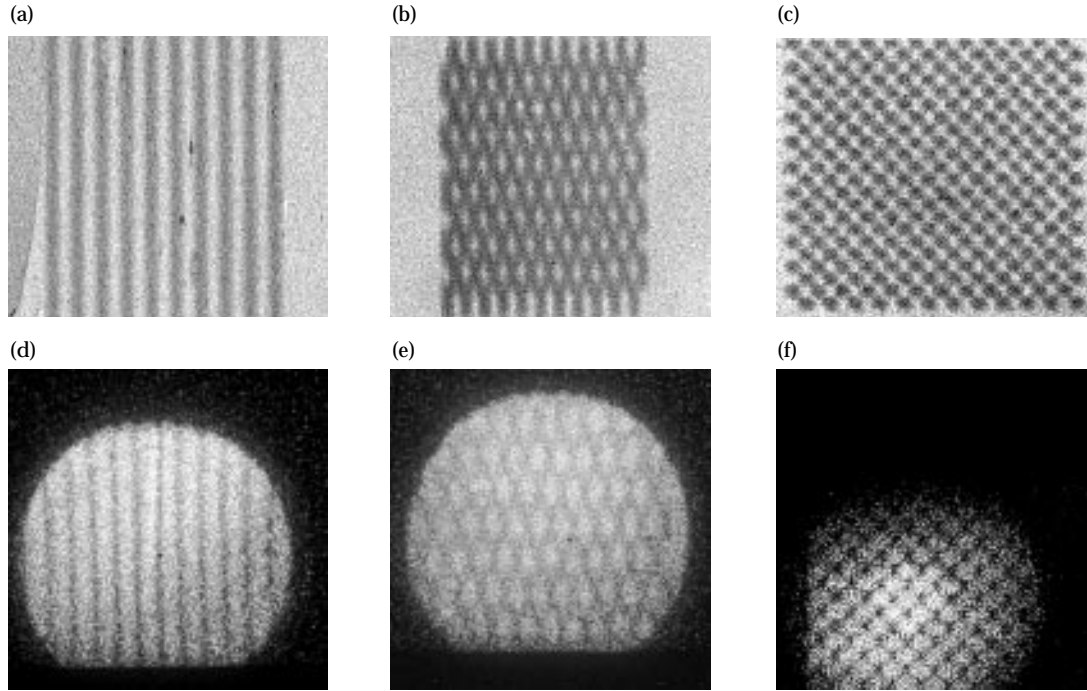


FIGURE 32. (a)–(c) Contact radiographs of foils identical to those used in the 3-D single-mode Nova experiments. Perturbations correspond to (a) 2-D $\lambda = 50 \mu\text{m}$, $\eta_0 = 2.5 \mu\text{m}$; (b) 3-D $k_x = 3k_y$, $\lambda_x = 53 \mu\text{m}$, $\lambda_y = 158 \mu\text{m}$, $\eta_0 = 2.4 \mu\text{m}$; and (c) 3-D $k_x = k_y$, $\lambda_x = \lambda_y = 71 \mu\text{m}$, $\eta_0 = 2.7 \mu\text{m}$. (d)–(f) Corresponding images from Nova shots at 4.3 ns. (20-03-0595-1390pb01)

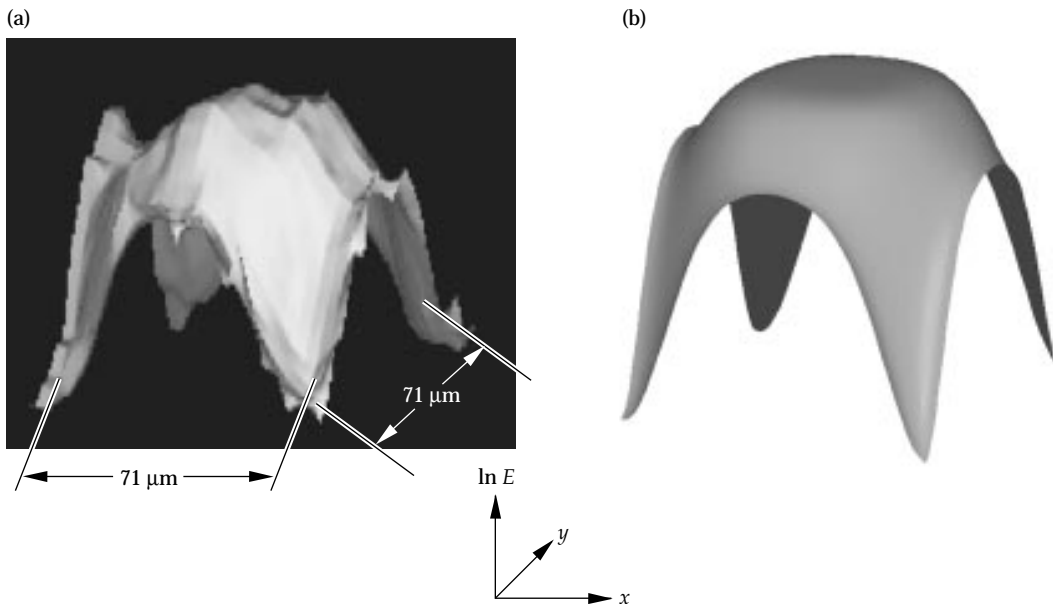


FIGURE 33. 3-D surface perspective of the $k_x = k_y$ case from Fig. 32 as (a) measured on the Nova shot at 4.3 ns and (b) simulated with the 3-D radiation–hydrodynamics code HYDRA.⁵³ The height is proportional to $\ln E$. (50-05-0595-1116pb01)

where subscripts 1 and 2 refer to the dense pusher fluid and low-density ablation plasma, respectively, V is the volume of fluid pushed aside by the bubble passage, S is the cross-sectional area of the bubble, and c_D is the drag coefficient. Equation (19) states that the net force on the mass $\rho_1 V$ of the heavy fluid equals the buoyancy force minus drag. The bubble tip naturally acquires the shape that minimizes the drag per unit mass, i.e., the bubble evolves towards a shape that minimizes S/V , which implies a spherical bubble tip shape, as observed. This is entirely equivalent to the common interpretation

that for a spherical 3-D bubble the flow can carry material away from the bubble tip on all sides, allowing it to transit more easily into the spike regions.^{51,56} One can also obtain from Eq. (19) the form of the terminal bubble velocity of Eq. (7). When buoyancy is exactly balanced by drag, one has $(\rho_1 - \rho_2) Vg = c_D \rho_1 u^2 S$. If we let $V \propto \lambda^3$, $S \propto \lambda^2$, and $\rho_2 \approx 0$, we then have $\rho_1 \lambda^3 g \propto c_D \rho_1 u^2 \lambda^2$; this yields $u^2 \propto g\lambda$, as in Eq. (7). Also note that if $g = 0$, as in the Richtmyer–Meshkov instability (long after shock passage), we obtain $u_{RM} \sim \lambda/t$, as pointed out by Alon et al.⁵⁵ and as was recently observed.⁵⁷

The images are Fourier analyzed, and the amplitudes corresponding to the fundamental mode are extracted. For an experimental demonstration of the effects of dimensionality on perturbation growth, we conducted shots for three targets (2-D $\lambda = 50 \mu\text{m}$, 3-D $k_x = k_y$ and $k_x = 3k_y$). The total laser energy for these shots was similar, and the timing and filtering of the diagnostic were identical. Figure 34(a) shows the results for the evolution of the fundamental mode. The $k_x = k_y$ square 3-D mode grows the most, the $\lambda = 50 \mu\text{m}$ 2-D mode

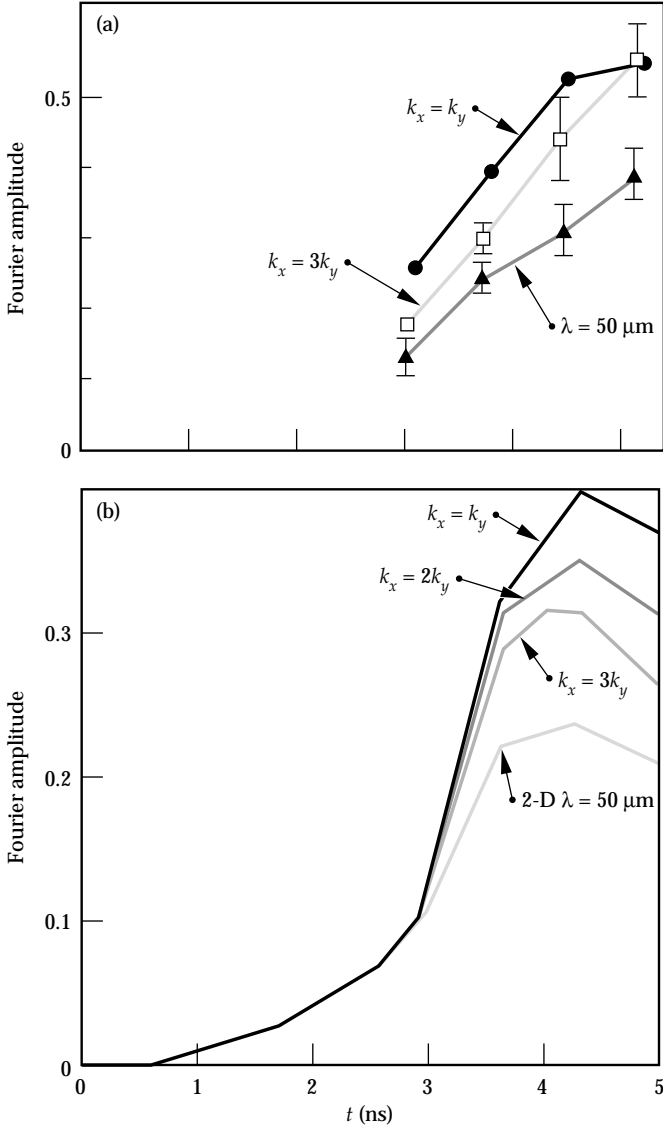


FIGURE 34. (a) Results of the evolution of the fundamental mode Fourier amplitude of $\ln E$ for the 3-D $k_x = k_y$, $k_x = 3k_y$, and 2-D $\lambda = 50 \mu\text{m}$ perturbations. Connecting lines are meant only to guide the eye. (b) Predicted Fourier amplitude of $\ln E$ from 3-D HYDRA simulations for the evolution of four perturbation shapes, all with the same wave vector magnitude $k = (k_x^2 + k_y^2)^{1/2}$, for somewhat different drive histories and foil thicknesses from those of (a). The most symmetric ($k_x = k_y$) mode is predicted to grow the most, the 2-D $\lambda = 50 \mu\text{m}$ mode to grow the least, and the 3-D stretched cases fall in between, in agreement with the experiments. (20-03-0595-1389pb01)

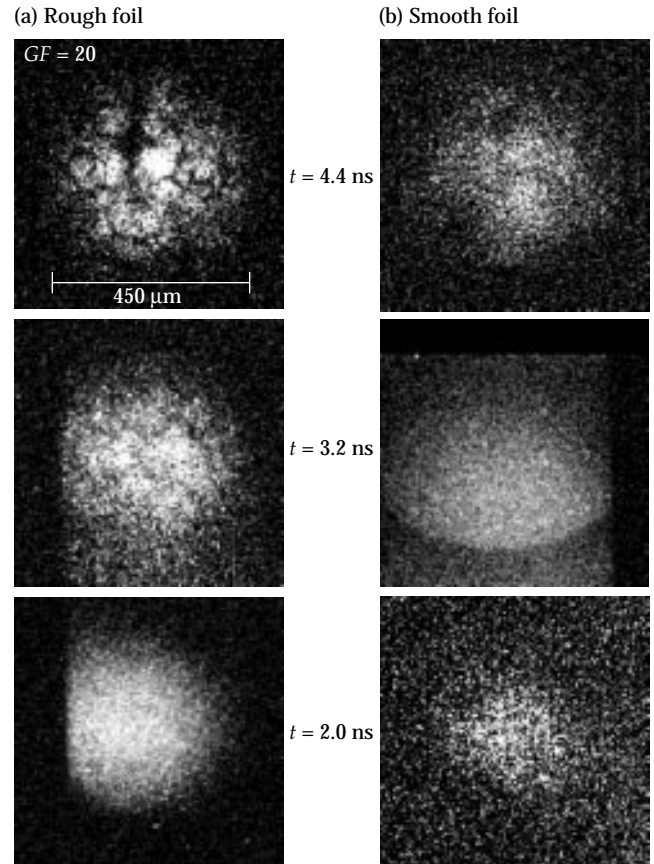


FIGURE 35. Typical 2-D images from surface-finish experiments using CH(Br) foils with two surface finishes, (a) rough ($\sigma_{rms} = 1.7 \mu\text{m}$) and (b) smooth ($\sigma_{rms} = 10 \text{ nm}$). The diagnostic was a gated x-ray framing camera filtered with $381 \mu\text{m}$ Be; foil was back-illuminated with x rays generated by a $\sim 500\text{-}\mu\text{m}$ -diam random phase plate (RPP)-smoothed laser beam incident on a Sc backlighter disk. (20-03-1293-4408pb01)

grows the least, and the $k_x = 3k_y$ stretched 3-D mode falls in between.

Figure 34(b) shows results from HYDRA simulations which were performed to help select parameters for the experiments. The foil thicknesses and drive histories in the experiments were somewhat different than those used in these simulations. The perturbations, in order of decreasing peak growth, correspond to $k_x = k_y$, $k_x = 2k_y$,

$k_x = 3k_y$, and 2-D $\lambda = 50 \mu\text{m}$. Our simulations clearly show that the most symmetric perturbations grow the most, as reported by others.^{23,56,58,59} This agrees qualitatively with our experimental observations; quantitative comparisons are under way.

Ultimately we are interested in the fully 3-D evolution at the ablation front of a perturbation consisting of a full continuum of modes. Recent progress has been made in developing 3-D modeling capability.^{5,51,53,56,58-61} We have therefore begun a series of surface-finish experiments to compare the perturbation growth from a randomly roughened surface with that from a smooth surface. We generated the rough surface by sand blasting a glass mold with 50- μm Al_2O_3 pellets. The typical deviation from the average for the smooth foil is $\sigma_{\text{rms}} = 10 \text{ nm}$, whereas $\sigma_{\text{rms}} = 1.7 \mu\text{m}$ for the rough foil.

Figure 35 shows gated images taken at 2.0, 3.2, and 4.4 ns when such foils were accelerated. Late in time, the surface of the rough foil has evolved into large, roughly hexagonal bubbles of transverse size $\sim 100 \mu\text{m}$. Figure 36(a) shows this more quantitatively in $\Delta \ln E \approx -\Delta \text{OD}$ profiles. These horizontal lineouts represent the central region of each image shown in Fig. 35; the late-time lineout contains the prominent central bubble at 4.4 ns. Figure 36(b) shows similar profiles for a standard smooth foil; there is no obvious perturbation growth into bubbles and spikes. Figure 37 shows the

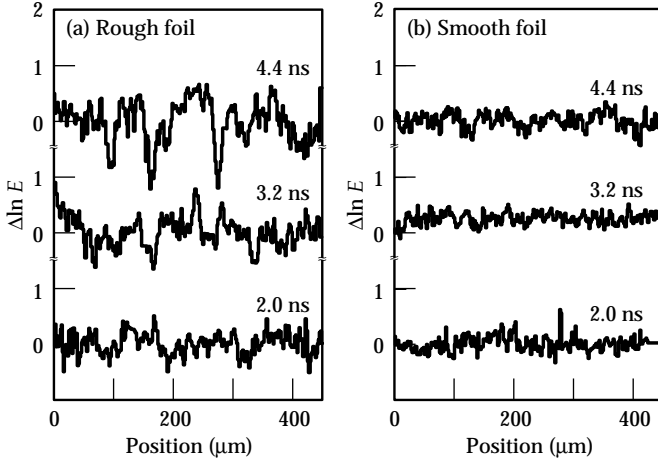


FIGURE 36. Corresponding $\Delta \ln E$ lineouts from Fig. 35 for (a) rough foil, (b) smooth foil. (20-03-0293-0379pb01)

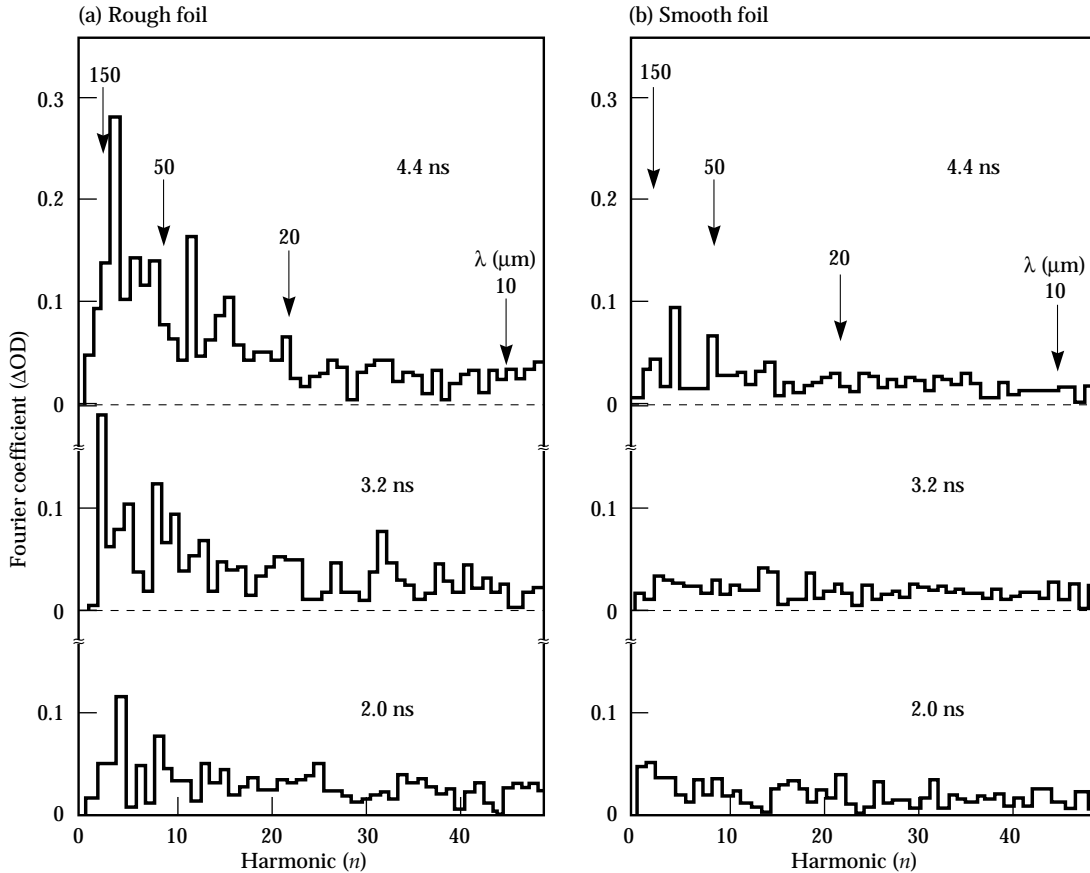


FIGURE 37. Absolute value of the real component of the Fourier transform of the $\Delta \ln E$ profiles shown in Fig. 36. Harmonic n and wavelength λ_n are related by $\lambda_n = (450 \mu\text{m})/n$, as indicated for a few cases by arrows. (20-03-1293-4409pb01)

corresponding Fourier transforms. The smooth foil again shows no significant growth. For the rough foil, the growth late in time is dominated by harmonics $n = 3$ – 8 , corresponding to $\lambda = 150$ – 56 μm . This is reasonable, because perturbations with $\lambda > 150$ μm grow too slowly, and perturbations with $\lambda < 56$ μm are more strongly ablatively stabilized [see Fig. 21(d)].

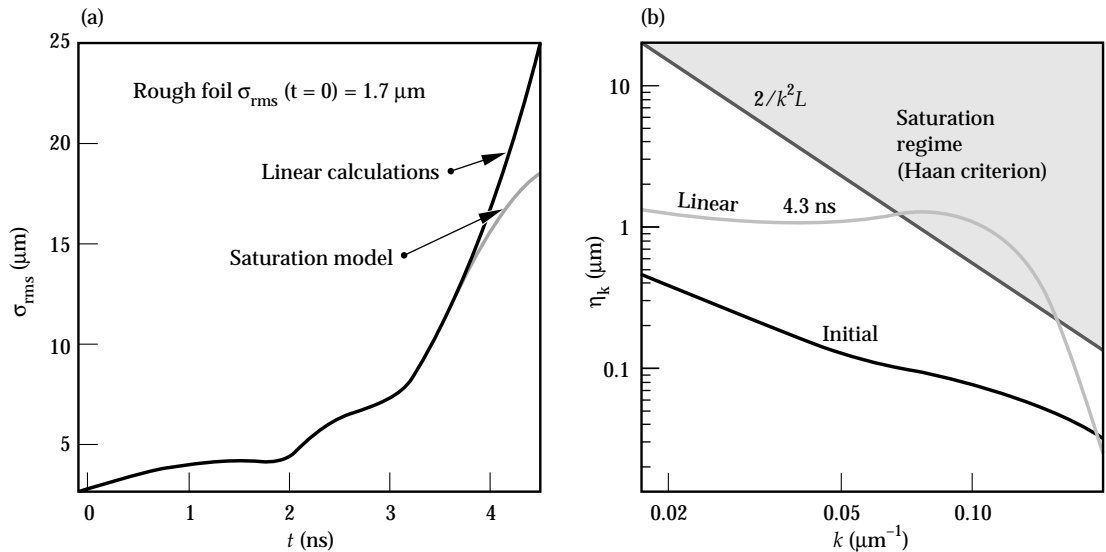
Late in time, the Fourier spectrum for the rough surface is dominated by the fourth harmonic, with peak amplitude $\eta = 0.28$. This fourth harmonic results from the prominent 112- μm -diam bubble shown in the center of the image at 4.4 ns in Figs. 35(a) and 36(a). We use this amplitude to make a crude estimate of growth factor in optical depth, G_{OD} , for the dominant mode. From the surface profile of a similar rough foil, we estimate $\eta_0(\lambda = 100$ $\mu\text{m}) \approx 0.3$ μm . The initial contrast for a CH(Br) foil with a $\lambda = 100$ μm , $\eta_0 = 5$ μm pure sinusoidal initial perturbation was measured on a separate shot (using the same diagnostic, backlighter, and filtering) to be $\Delta\text{OD}_0 = 0.14$. We therefore estimate the growth factor for the dominant mode in Fig. 37(a) to be $G_{\text{OD}} = \eta/\eta_0 \approx 0.28/[(0.14)(0.3$ $\mu\text{m})/(5.0$ $\mu\text{m})] = 33$. This is considerably less than expected in a typical implosion, but it represents a first step towards experimentally addressing the question of 3-D growth from a random initial surface finish. An analysis based on 2-D LASNEX simulations and Haan's 3-D saturation theory³² has been done for this rough surface experiment. The results, shown in Fig. 38, suggest that the multimode RT evolution was just entering the saturation regime, according to Haan's criterion. We are therefore designing a drive to produce a higher growth factor and having a longer acceleration interval, to allow a more discriminating test of multimode saturation physics.

The RT Instability in Cylindrical Implosions

The RT growth during ablative acceleration has been measured in many direct- and indirect-drive experiments. These measurements have verified the predicted stabilizing effect of mass ablation and density gradients. But few of these experiments have examined the role of feedthrough or of the deceleration phase, during which the growing perturbations may enhance thermal losses from the "hot spot" or reduce the efficiency of compressional work done by the shell on the fuel. Qualitatively, RT growth on the inner surface during deceleration differs from growth on the outer surface during acceleration by the lack of ablative stabilization. The RT growth at the inner surface is moderated, however, by the density gradient. In addition, convergent effects are important during these three phases. During ablative acceleration, convergence introduces a different threshold for nonlinear effects because of a decrease of perturbation wavelength in time,³² thin-shell effects,^{7,29,62} and a change in perturbation amplitude arising from the combination of convergence and compressibility.⁶³ Feedthrough is decreased because the pusher shell thickens during convergence. Convergence effects are magnified during deceleration.^{5,32,61,63}

Current designs for indirectly driven ignition capsules⁴¹ operate near the edge of present capabilities to fabricate smooth surfaces. It is important to assess the magnitude of feedthrough in ICF implosions if we are to correctly model the relative roles of perturbations on the outer and inner surfaces of capsules for these capsule designs. The effect of convergence on feedthrough is an integral part of the problem, so experiments in

FIGURE 38. Saturation analysis based on 2-D LASNEX simulations and the Haan 3-D saturation theory³² for the rough surface foils, shown in terms of (a) σ_{rms} vs time and (b) Fourier spectrum at peak growth. (20-03-1293-4501pb02)



convergent geometry are desirable. Few experiments to study convergent RT instability have been performed⁶⁴ because of the difficulty of diagnosis. Perturbations and mixing-layer widths are difficult to measure in spherical geometry because of the lack of a direct line of sight and because of errors associated with Abel inversions in spherical geometry near peak convergence. Although perturbation growth can be indirectly inferred from time-dependent x-ray spectral line ratios in spherical implosions,^{18,19,65} the results depend on the details of difficult atomic physics and radiative transport calculations. We have used an indirectly driven cylindrical configuration to allow diagnostic access and superior control of the shell's inner surface during target fabrication, although questions arise concerning edge effects and implosion symmetry. We chose a feedthrough experiment to demonstrate that quantitative RT experiments can be performed in cylindrical geometry and to measure feedthrough in a radiation-driven target for the first time.

Figure 39 shows the experiment geometry. The cylindrical polystyrene shell was mounted orthogonal to the hohlraum axis, to allow a direct line of sight to the diagnostics, to avoid interference with laser beams, and to avoid radiation flow into the ends of the cylinder (as may occur in a coaxial configuration). Eight 351-nm, 2.5-kJ, 2.2-ns Nova drive beams are pointed symmetrically about the cylinder. A low-adiabat drive was used, consisting of a low-power foot followed by a ramp to higher power, with a peak-to-foot ratio of about 3. A separate 528-nm, 2-ns beam was used to irradiate a 2-mm-diam Ag disk to create an x-ray backlighter of photon energy $\sim 3\text{--}3.6$ keV. An RPP⁶⁶ was used to smooth the beam intensity onto the Ag disk, and the

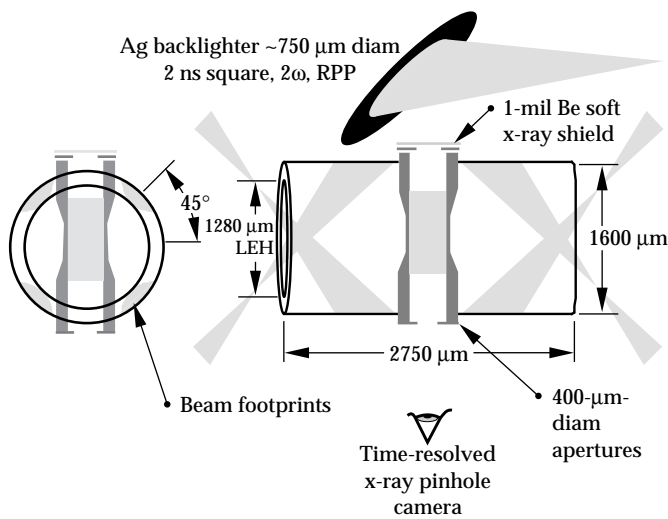


FIGURE 39. Side and transverse views of experimental geometry for the cylindrical implosion Rayleigh-Taylor experiment. (20-03-0895-2048pb01)

resultant laser spot was ~ 750 μm in diameter. The disk was located ~ 3.5 mm away from the center of the cylinder and was oriented so that the disk normal bisected the angle between the cylinder axis and the backlighter laser direction. A 1-mil Be foil was placed between the backlighter and cylinder to filter out soft x rays and to keep reflected 2ω light from the backlighter from striking the inside of the cylinder. There should be no 2ω unconverted light from the eight Nova drive beams with a line of sight to the cylinder, so a Be shield on the other side of the cylinder is unnecessary.

Figure 40 shows the polystyrene cylinder in detail. The cylinder has an outer diameter of 630 μm , an inner diameter of 430 μm , and length of 1800 μm . The outer diameter is tapered toward the center of the cylinder, allowing the central region of the cylinder to implode before the ends and minimizing edge effects. Perturbations were machined onto the outer surface of the central 400- μm -long region of the cylinder in a dodecagon shape (fundamental mode number $m = 12$). (A sine wave perturbation would be preferable, because it contains no harmonics, but a sine wave is much more difficult to fabricate than a dodecagon.) A 4- μm -thick, 160- μm -long dichlorostyrene ($\text{C}_8\text{H}_6\text{Cl}_2$) belt was placed around the center of the cylindrical shell, flush with the shell's inner surface. The belt served as a marker layer, because it is opaque to the x-ray backlighter, whereas the polystyrene cylinder is relatively transparent. The time-resolved pinhole camera diagnostic images the marker layer; late in time, it also images some of the surrounding compressed material. The marker layer is on the inner surface of the cylinder and has no initial perturbations, so any perturbations observed indicate feedthrough of the initial outer-surface perturbations to the inner surface. The marker

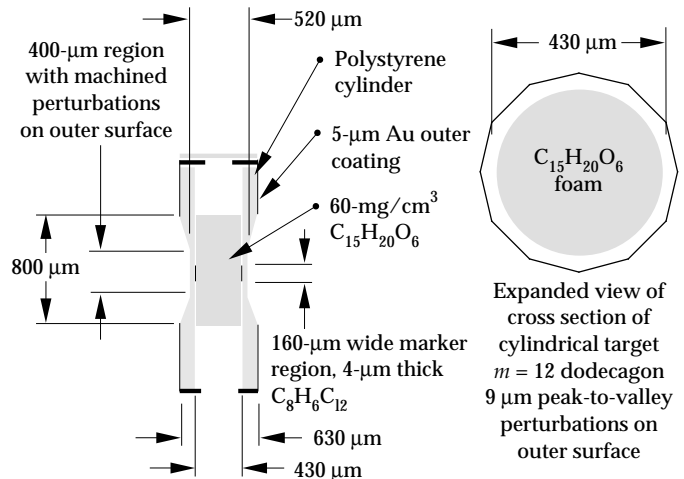


FIGURE 40. Side and end views of target of Fig. 39. (20-03-0895-2049pb01)

layer has a density close to that of the unchlorinated polystyrene (1.4 g/cm^3 vs 1.0 g/cm^3); calculations show that this slight density mismatch does not cause significant RT growth. A 60-mg/cm^3 microcellular triacrylate foam ($\text{C}_{15}\text{H}_{20}\text{O}_6$) is placed inside the shell to provide a back-pressure as the cylinder implodes. The foam has a cell size $\sim 1\text{--}3 \mu\text{m}$. The foam is shorter than the cylinder to minimize opacity to the backlighter. The cylinder is fabricated by coating the marker layer on a mandrel, machining the marker layer to size, coating the other polymer layers onto the mandrel and marker layer, machining the coatings, leaching the mandrel out, inserting the cylinder inside the hohlraum, and inserting the foam inside the cylinder. On each end of the cylinder, a $400\text{-}\mu\text{m}$ -diam circular aperture made of $25\text{-}\mu\text{m}$ -thick gold was placed concentric with the cylinder axis. These apertures prevented any x rays emitted by the walls of the cylinder from entering the pinhole camera diagnostic, provided an alignment and parallax diagnostic on the shot, and provided a centering fiducial for each frame on the pinhole camera. The fiducial is crucial for quantitative Fourier analysis of the data.

The cylinder was viewed along its axis with a time-resolved, gated x-ray pinhole camera (GXI).⁶⁷ A 4×4 pinhole array with pinhole diameters of $\sim 7 \mu\text{m}$ allowed 16 images spaced $\sim 55 \text{ ps}$ apart to be projected onto four microchannel-plate strip lines with a magnification of 12. The filters used were $12.7\text{-}\mu\text{m}$ Ti and $150\text{-}\mu\text{m}$ Be. The Ti was chosen to block x rays with energies above 4.75 keV and to allow the silver L-shell backlighter radiation through.

To determine the contrast ratio expected between the tracer layer and the central foam region, a backlit nonimplosion shot was taken with a $40\text{-}\mu\text{m}$ -thick piece of chlorinated polystyrene on top of part of the foam. The contrast in exposure was measured to be 16:1 after a density-to-exposure correction of the film. A streaked x-ray crystal (KAP) spectrometer viewed the Ag backlighter disk and provided the backlighter spectrum as a function of time. Figure 41 shows a measured backlighter spectrum on an implosion shot. The opacity of cold chlorinated polystyrene and the gold photocathode GXI response are overlaid. The chlorinated polystyrene absorbs virtually all the Ag L-shell radiation, and the GXI detects most of the backlighter where there is no chlorinated polystyrene. The transmission of 3.5-keV x rays through $100 \mu\text{m}$ of cold polystyrene is ~ 0.6 . Figure 42 shows the total 3ω laser power into the hohlraum and the spectrally integrated x-ray backlighter flux as a function of time. The GXI is timed to measure during the peak x-ray backlighter fluence. The hohlraum was viewed along its axis with the west axial x-ray imager (WAX)⁶⁸, another time-resolved pinhole camera with a serpentine microchannel plate strip. This

was used to verify that there was no beam clipping on the laser entrance holes.

One purpose of a narrow $160\text{-}\mu\text{m}$ tracer region is to minimize the effect of misalignment on the pinhole camera measurement of the interface location. For example, a 1° tilt in the cylinder with respect to a point on the GXI would result in a lateral spread of $2.8 \mu\text{m}$ in an interface. Since the pinhole array also has a lateral spread in location, there is parallax between images. For a perfectly aligned cylinder, the four center pinholes have a parallax of 0.9° , the next eight surrounding pinholes have a parallax of 2° , and the four corner pinholes have a parallax of 2.7° . The alignment of the cylinder relative to the GXI, measured on a shot with fiducial wires across the front and back faces of the cylinder, was $0.4^\circ \pm 0.6^\circ$. Thus the lateral spread in an image is primarily due to parallax.

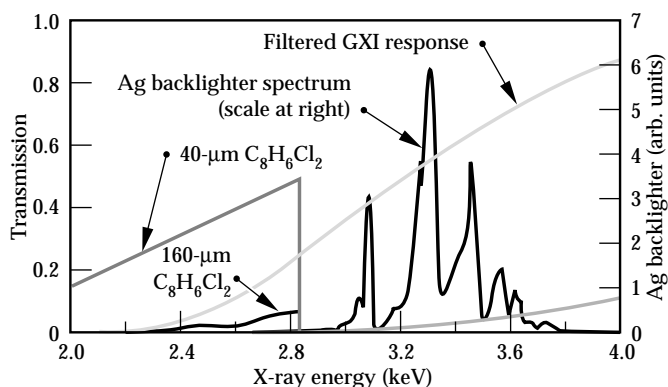


FIGURE 41. The measured x-ray spectrum of the Ag backlighter compared with the gated x-ray imager spectral response and the transmission assuming cold opacities of the tracer layer. $160 \mu\text{m}$ is the initial length of the marker layer, and $40 \mu\text{m}$ represents an expansion of the marker layer by a factor of 4. (20-03-1095-2284pb01)

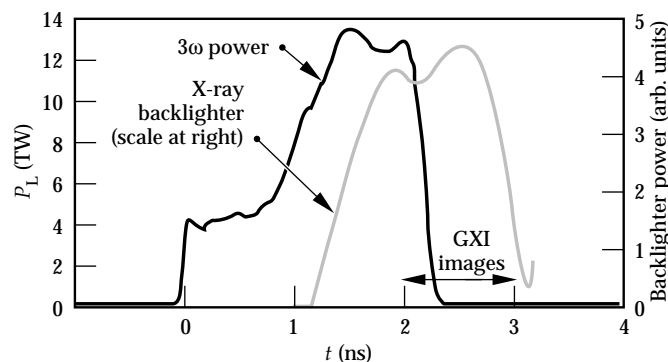


FIGURE 42. The 3ω ($\lambda = 351 \text{ nm}$) power of eight Nova laser beams (left scale) and x-ray backlighter power (right scale). The x-ray images are taken between 2 and 3 ns, near the peak of the backlighter emission. (20-03-1095-2285pb01)

Figure 43 shows 12 frames from an implosion with the initially perturbed surface described above. The $m = 12$ perturbation is clearly visible. The perturbation amplitude grows in time, and the wavelength decreases as the radius decreases. At $t = 2.11$ ns (first image), calculations indicate that the ablation front has not burned through to the marker layer, so the observed $m = 12$ feature is the result of feedthrough of the initial perturbation to the marker layer. The tips of the dodecagon have grown into spikes at the ablation front. Figure 44(a), an image of an unperturbed cylindrical implosion under identical conditions to a perturbed implosion [Fig. 44(b)], shows no $m = 12$ perturbations. The absence of any $m = 12$ feature in this case verifies that the initial perturbations caused the observed feedthrough. (We attribute the small bump at the upper left of the unperturbed shell to a target defect).

In the perturbed image [Fig. 44(b)], we identify a contour $r(\theta)$ at the outer edge at about the 50% exposure level and draw it in [Fig. 45(a)]. The contour can then be fitted with a Fourier series according to the usual prescription

$$r(\theta) = \frac{a_0}{2} + \sum_{m=1}^{\infty} (a_m \cos m\theta + b_m \sin m\theta),$$

where

$$a_m = \frac{1}{\pi} \int_{-\pi}^{\pi} r(\theta) \cos m\theta d\theta$$

and

$$b_m = \frac{1}{\pi} \int_{-\pi}^{\pi} r(\theta) \sin m\theta d\theta.$$

The results of the fit are shown in Fig. 45(b) and the Fourier composition is shown in Fig. 46, where the modal amplitude $(a_m^2 + b_m^2)^{1/2}$ is plotted vs mode number m . The term a_0 represents the average diameter of the contour, and a_1 and b_1 represent the offsets of the center of the contour from the axes of symmetry. The coefficients depend on the choice of the center of the contour. We examined several methods to choose the center of the contour: a least-squares fit to a circle, a minimization of a_1 and b_1 , and a center based on the measurement of the center of the defining aperture. Of these methods,

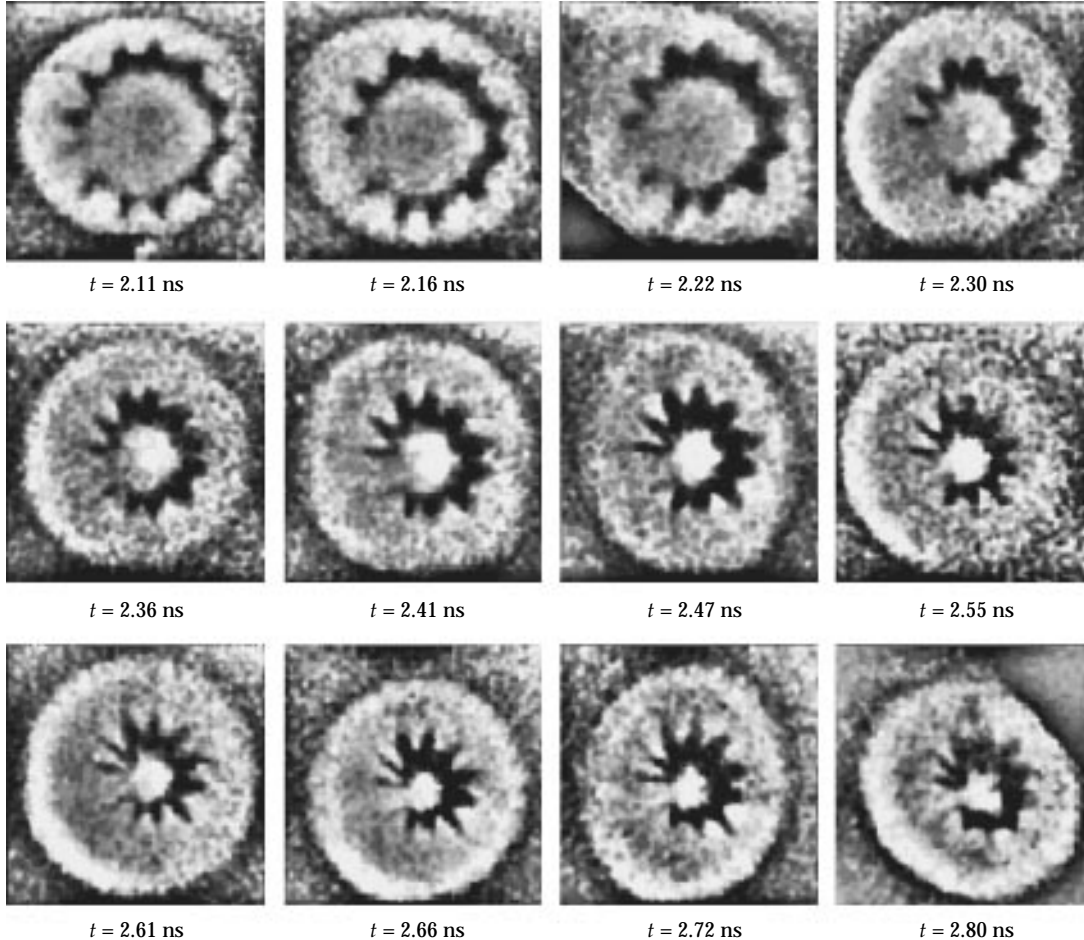


FIGURE 43. A sequence of gated x-ray images of the cylindrical backlight implosion from one experiment ($t = 0$ corresponds to the start of the laser pulse). Shock emission appears on center at 2.30 ns. The backlighter spatial extent is limited by the circular apertures at each end of the cylinder, and the deviation from circularity is a measure of the effect of parallax. (20-03-0895-2050pb01)

only the latter proved reliable and resulted in mode number conservation during the implosion. Figure 47 shows images of the perturbed implosion later in time. One side of the target has imploded closer to the center than the other side. This is probably due to a slight manufacturing imperfection in the target, as if the marker layer were thinner on one side than on the other. The apertures also indicate, on each image, the parallax due to the offset of each pinhole from the axis of the cylindrical shell; the images can be corrected for this effect.

At 2.11 ns, there are significant components at $m = 1, 4, 8$, and 12. Mode 1 exists because one side of the cylinder implodes faster than the other. Mode 4 is expected because of the discrete number of beams illuminating the hohlraum. Mode 2 was minimized by the proper choice of beam pointing. Mode 12 has an amplitude of $\eta = 10 \mu\text{m}$. Since the instrumental resolution is insufficient to distinguish between mode 12 and modes 11

and 13, it is reasonable to expect that the effective amplitude of the perturbation at mode 12 is the quadrature sum of modes 11, 12 and 13, resulting in an amplitude of $12 \mu\text{m}$. Other methods of analysis, including curve fits to the functional form

$$r(\theta) = \frac{a_0}{2} + \sum_{n=1}^4 (a_n \cos 12nx + b_n \sin 12nx)$$

and variations in the choice of a center, result in a mode-12 amplitude of $9\text{--}11 \mu\text{m}$; we assign the value $10 \pm 2 \mu\text{m}$ as the amplitude of mode 12. A Fourier analysis of a dodecagon inscribed in a $260\text{-}\mu\text{m}$ -radius circle gives amplitudes of 3.5, 0.85, and $0.34 \mu\text{m}$ for modes 12, 24, and 36 respectively. Thus at $t = 2.11 \text{ ns}$, the fundamental has grown by a factor of 2.9 ± 0.6 with respect to its initial value.

To test the sensitivity of the analysis to the choice of 50% isodensity contour, we analyzed several images with isodensity contours ranging from 40% to 60%.

FIGURE 44. (a) Gated x-ray image of an implosion taken with a target with no initial perturbations and (b) an otherwise identical implosion taken with a dodecagon initial perturbation. Images taken $t = 2.16 \text{ ns}$. (20-03-0895-2053pb01)

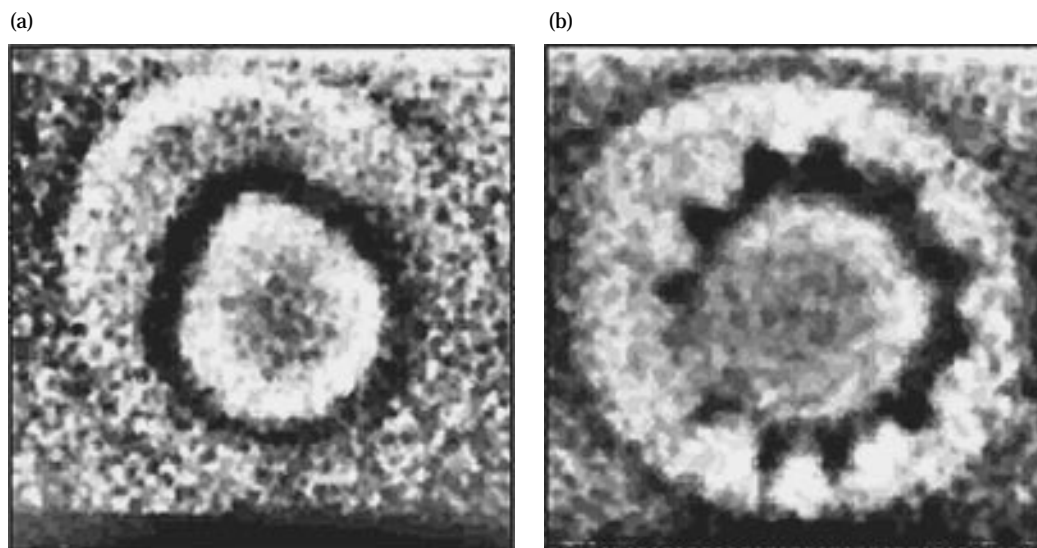
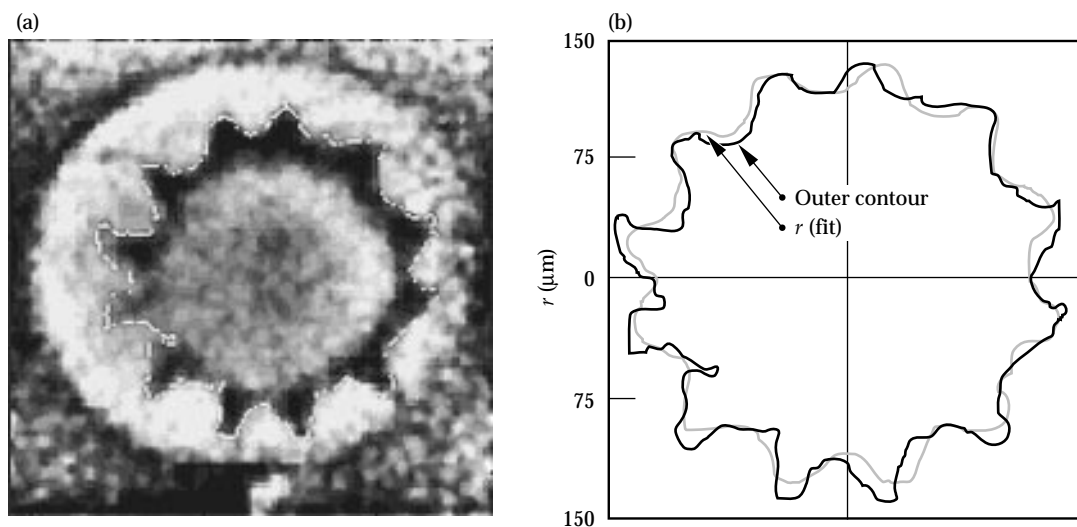


FIGURE 45. (a) An outer contour taken at 50% peak exposure, superposed over the initial x-ray image taken at 2.11 ns. (b) Results of a Fourier series fitted to the contour shown in (a). The horizontal and vertical axes are equal, each covering a range of $300 \mu\text{m}$. (20-03-0895-2053pb02)



The results were insensitive to choice of isodensity contour. For isodensity values outside this range, the background noise from the microchannel plate occasionally affected the contour, with unphysical contours appearing because of noise spikes.

For each image, we Fourier analyzed the contours for the inner edge of the marker layer (the interface between the marker layer and the TPX foam) and the outer edge (the interface between the marker layer and surrounding polystyrene cylinder). Figure 48 shows the time dependence of $a_0/2$, which represents the average radius. The implosion trajectory is consistent with a 195-eV peak drive temperature in a calculation with the 1-D radiation-hydrodynamic code HYADES.⁶⁹

The perturbation was initialized in its linear regime. At $t = 0$, the wavelength of mode $m = 12$ is $\lambda = 2\pi R/m = 136 \mu\text{m}$, where $R = 260 \mu\text{m}$. The amplitude of mode $m = 12$ is $\eta_0 = 3.50 \mu\text{m}$ initially, so that

$\eta/\lambda = 0.026$. At 2.11 ns, the radius of the shell is $R = 122 \mu\text{m}$, so that $\lambda = 2\pi R/m = 64 \mu\text{m}$. The amplitude of mode $m = 12$ is $\eta = 10 \mu\text{m}$, so $\eta/\lambda = 0.16$. The perturbation at the marker layer has exceeded the nominal threshold for nonlinearity $\eta/\lambda \approx 0.1$ at 2.11 ns.

Growth of perturbations on the marker layer result both from shock imprinting and from feedthrough from RT growth at the ablation front. Simple estimates suggest that the latter dominates. To illustrate this, we estimate the marker layer amplitude that would result from shock imprinting alone. The shock is launched from a rippled surface at the ablation front, and hence is itself rippled. A rough estimate of the amplitude of the ripple imparted to the marker layer upon passage of the rippled shock is given by

$$\eta_m = \eta_0(1 - \Delta R_0/\lambda_0)u_p/v_s.$$

Here η_m is the amplitude of the imprinted ripple on the marker layer, η_0 is the ablation front surface

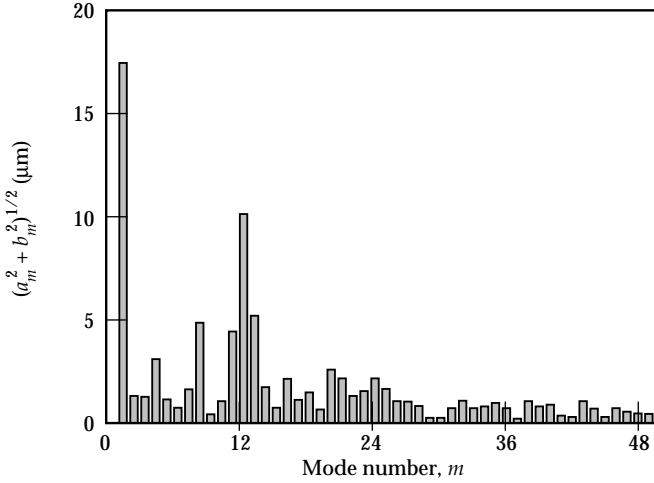


FIGURE 46. Fourier amplitudes vs mode number m for a 50% outer contour of the gated x-ray image at $t = 2.11$ ns. The largest physically significant amplitude corresponds to $m = 12$. (20-03-1095-2286pb01)

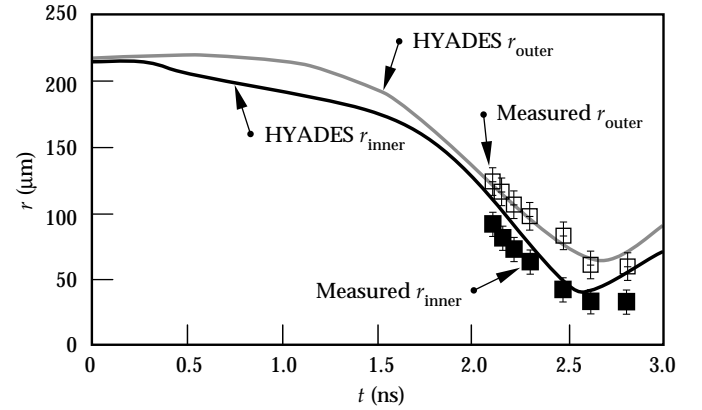


FIGURE 48. Measured outer and inner diameters of the tracer layer vs time, and corresponding trajectories from a HYADES calculation. (20-03-0895-2052pb01)

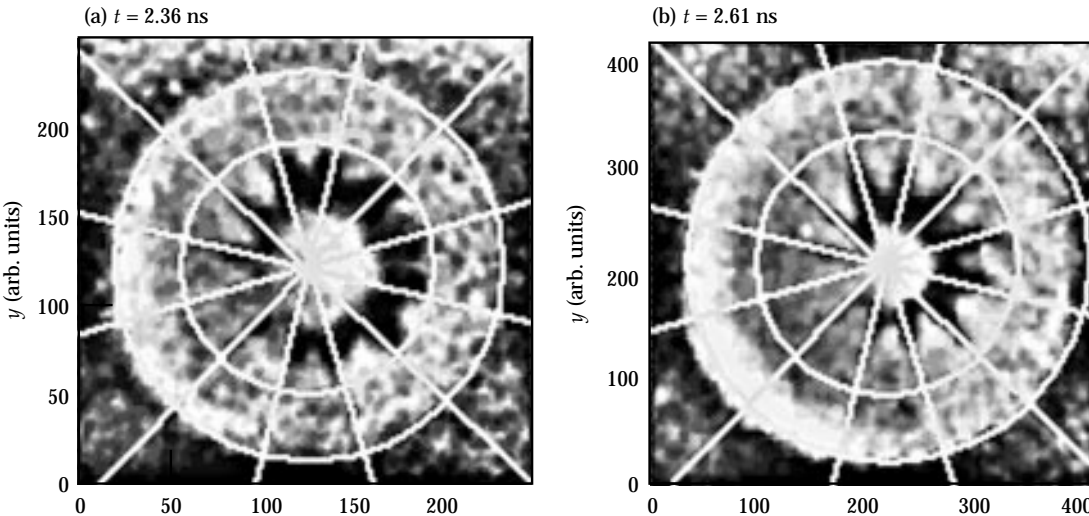


FIGURE 47. Gated x-ray images at (a) 2.36 and (b) 2.61 ns, with a mode 12 uniform in angle grid superposed. Outermost circular contour is a fit to the 400- μm -diam Au defining aperture in both images. One side of the target has imploded faster than the other, yet the mode number is preserved using a center corresponding to the original cylinder axis. (20-03-1095-2295pb01)

perturbation initial amplitude, ΔR_0 is the initial distance from the ablation front to the marker layer, λ_0 is the initial perturbation wavelength, u_p the particle velocity behind the shock front, and v_s the shock velocity. The factor $\eta_0(1-\Delta R_0/\lambda_0)$ is an estimate, based on the shock oscillation data of Endo et al.,²² of the amplitude of the shock-front ripple, assuming that it reverses phase after having traveled a distance of λ_0 . Since $\Delta R_0 \approx 40 \mu\text{m}$ and $\lambda_0 \approx 100 \mu\text{m}$, the rippled shock has not reversed phase by the time it reaches the marker layer, but its amplitude is $\sim 40\%$ lower than η_0 . Assuming that this marker layer perturbation then grows linearly in time via the Richtmyer–Meshkov instability, we write

$$\eta_{12}(t) = \eta_m + \eta_m A^* k u_p \Delta t,$$

where $\eta_{12}(t)$ is the amplitude of the fundamental mode at time t , A^* is the post-shock Atwood number, and $\Delta t = t - t_s$, where $t_s = 0.4 \text{ ns}$ is the time when the first shock reaches the marker layer. Using reasonable estimates for the various parameters in this equation, we estimate that $\eta_{12}(2.11 \text{ ns}) \approx 2.5 \mu\text{m}$. Allowing for some additional growth due to the higher u_p after the second shock reaches the marker layer at 1.6 ns , we get $\eta_{12}(2.11 \text{ ns}) \approx 3 \mu\text{m}$. The measured amplitude of $10 \mu\text{m}$ at 2.11 ns is considerably larger, suggesting that feedthrough from RT growth at the ablation front is the dominant source of the observed growth.

During deceleration, the inner surface becomes RT unstable and perturbations fed through to the inside surface grow without ablative stabilization. At 2.72 and 2.80 ns (Fig. 43), visible spikes protrude into the core. The spikes on the inner edge of the marker layer correspond radially to bubbles on the outer surface, such as can be seen in Fig. 43 at 2.30 ns and 2.47 ns . This suggests that ablation-front bubble growth is the dominant feed-through mechanism.

Summary

We have conducted an extensive series of experiments and simulations to examine the growth of single modes over a range of wavelengths and to examine the effect of multiple modes on perturbation growth. For single modes, the perturbation evolves before shock breakout because of the rippled shock dynamics. After shock breakout, the perturbations grow rapidly in the linear regime and saturate in the nonlinear regime, with the appearance of higher harmonics. In multimode foils, the individual modes grow independently in the linear regime. In the nonlinear regime, the modes become coupled and $k_i \pm k_j$ terms are clearly observed, in agreement with simulations and second-order perturbation theory. Mode coupling redistributes the perturbation in Fourier space, which in physical space corresponds to a change in perturbation shape. The bubbles become

broader and flatter and the spikes narrower. In terms of a continuum model, the individual modes of the 2-D perturbation saturate when they exceed $S_k = v_{2D}/k^{3/2}L^{1/2}$ in amplitude. The simulations systematically predict slightly more growth than is observed. This could be caused by greater than expected preheat in the foot of the drive, a stiffer EOS for CH(Br), or a degraded instrumental MTF.

Single-mode experiments very clearly indicate the differences between 2-D and 3-D perturbation shape. Axisymmetric 3-D bubbles grow the largest in the nonlinear regime, consistent with a simple buoyancy-vs-drag argument, third-order perturbation theory, and with full 3-D radiation–hydrodynamics simulations. The obvious next step is to measure the full multimode 3-D perturbation evolution and to compare the results with 3-D simulations and with the predictions of Haan’s saturation theory.

In radiation-driven cylindrical implosions, we have observed the RT instability seeded by feedthrough from the outer surface to the inner surface. The mode number was conserved during the implosion. This proof-of-principle cylindrical experiment shows the potential for new studies of RT instability in convergent geometry. Ablation-front growth and feedthrough were measured. With higher resolution, studies of the stagnation phase and inner surface breakup may be possible.

Appendix: Amplitude of Coupled Modes

Following Ref. 26, a solution to a second-order perturbation expansion of the 3-D hydrodynamic equations for inviscid, incompressible fluids can be written as

$$\eta_{\mathbf{k}}(t) = \eta_{\mathbf{k}}^L(t) + 2Ak \sum_{\mathbf{k}_2} \eta_{\mathbf{k}_2}^L(t) \eta_{\mathbf{k}-\mathbf{k}_2}^L(t) G(\mathbf{k}, \mathbf{k}_2) H(\mathbf{k}, \mathbf{k}_2, t), \quad (\text{A1})$$

where $\mathbf{k}' = \mathbf{k} - \mathbf{k}_2$ and where superscript L designates results in the linear regime. The time-independent part of the kernel $G(\mathbf{k}, \mathbf{k}_2)$ is given by

$$G(\mathbf{k}, \mathbf{k}_2) = \frac{1}{2} \frac{\gamma_2^2(1 - \hat{\mathbf{k}}_2 \cdot \hat{\mathbf{k}}) + \frac{1}{2}\gamma_2\gamma_2'(1 - \hat{\mathbf{k}}_2 \cdot \hat{\mathbf{k}}_2 - 2\hat{\mathbf{k}}_2 \cdot \hat{\mathbf{k}})}{(\gamma_2 + \gamma_2')^2 - \gamma^2(k)}, \quad (\text{A2})$$

where $\mathbf{k} = (k_x, k_y)$ is the perturbation wave vector, $\hat{\mathbf{k}} = \mathbf{k}/k$ is the unit vector, and $\gamma(\mathbf{k})$, γ_2 , and γ_2' are the linear growth rates for perturbations with wave vectors \mathbf{k} , \mathbf{k}_2 , and \mathbf{k}' , respectively. This weakly nonlinear theory is valid only so long as the dominant modes are not being changed significantly by the nonlinear terms. The full expression for $H(\mathbf{k}, \mathbf{k}_2, t)$ is complicated, but for the regime considered here we have $H \approx 1$.

Considerable simplification occurs for 2-D cosine perturbations with Atwood number $A = (\rho_1 - \rho_2)/(\rho_1 + \rho_2) \approx 1$. If we assume that $\gamma_k \propto k^{1/2}$, then Eq. (A1) reduces to

$$\eta_k \approx \eta_k^L + \frac{1}{2} k \left(\sum_{k'} \eta_{k'}^L \eta_{k+k'}^L - \frac{1}{2} \sum_{k' < k} \eta_{k'}^L \eta_{k-k'}^L \right), \quad (\text{A3})$$

where $k, k' > 0$, and the time dependence has been dropped from the notation for simplicity. For example, Eq. (5b) for the second harmonic of a single-mode perturbation, $\eta_2 \approx \frac{1}{2} k_1 \eta_1^2$, comes from the second term in the summation in Eq. (A3), where $k = 2k_1$ and $k' = k_1$.

Another simple case of general interest arises for $k = k_3 \pm k_2$. Here, Eq. (A3) reduces to

$$\eta_{k_3 \pm k_2} \approx \mp (k_3 \pm k_2) \eta_{k_2}^L \eta_{k_3}^L, \quad (\text{A4})$$

where $\eta_{k_n}^L$ represents the spatial amplitude attained by mode k_n had the growth been entirely in the linear regime.

Notes and References

1. S. Chandrasekhar, *Hydrodynamic and Hydromagnetic Stability* (Oxford U. P., London, 1968), Ch. 10; Lord Rayleigh, *Scientific Papers*, Vol. II (Cambridge U. P., Cambridge, 1900), p. 200; G. I. Taylor, *Proc. Roy. Soc. A* **201**, 192 (1950).
2. R. D. Richtmyer, *Commun. Pure Appl. Math.* **13**, 297 (1960); E. E. Meshkov, *Izv. Akad. Nauk. SSSR, Mekh. Zhidk. Gaz.* **5**, 151 (1969) (translation, NASA TTF-13-074, 1970).
3. J. D. Lindl and W. C. Mead, *Phys. Rev. Lett.* **34**, 1273 (1975).
4. E. Gamaly, "Hydrodynamic Instability of Target Implosions in ICF," in *Nuclear Fusion by Inertial Confinement: A Comprehensive Treatise*, G. Velarde, Y. Ronen, and J. M. Martinez-Val, Eds. (CRC Press, Boca Raton, 1993), p. 321.
5. H. Sakagami and K. Nishihara, *Phys. Rev. Lett.* **65**, 432 (1990); *Phys. Fluids B* **2**, 2715 (1990).
6. S. E. Bodner, *Phys. Rev. Lett.* **33**, 761 (1974).
7. R. L. McCrory, L. Montierth, R. L. Morse, and C. P. Verdon, *Phys. Rev. Lett.* **46**, 336 (1981).
8. H. Takabe, K. Mima, L. Montierth, and R. L. Morse, *Phys. Fluids* **28**, 3676 (1985); D. H. Munro, *Phys. Rev. A* **38**, 1433 (1988); M. Tabak, D. H. Munro, and J. D. Lindl, *Phys. Fluids B* **2**, 1007 (1990).
9. A. Caruso, V. A. Pais, and A. Parodi, *Laser Part. Beams* **10**, 447 (1992).
10. J. Grun et al., *Phys. Rev. Lett.* **58**, 2672 (1987).
11. M. Desselberger, O. Willi, M. Savage, and M. Lamb, *Phys. Rev. Lett.* **65**, 2997 (1990); M. Desselberger, O. Willi, M. Savage, and M. Lamb, *Phys. Fluids B* **5**, 896 (1993).
12. S. G. Glendinning et al., *Phys. Rev. Lett.* **69**, 1201 (1992).
13. J. D. Kilkenny, *Phys. Fluids B* **2**, 1400 (1990).
14. B. A. Remington et al., *Phys. Rev. Lett.* **67**, 3259 (1991); B. A. Remington, S. W. Haan, S. G. Glendinning, J. D. Kilkenny, D. H. Munro, and R. J. Wallace, *Phys. Fluids B* **4**, 967 (1992).
15. B. A. Remington et al., *Phys. Fluids B* **5**, 2589 (1993).
16. Guy Dimonte and Bruce Remington, *Phys. Rev. Lett.* **70**, 1806 (1993).
17. B. A. Hammel et al., *Phys. Fluids B* **5**, 2259 (1993); B. A. Hammel, J. D. Kilkenny, D. Munro, B. A. Remington, H. N. Kornblum, T. S. Perry, D. W. Phillion, and R. J. Wallace, *Phys. Plasmas* **1**, 1662 (1994).
18. B. A. Hammel et al., *J. Quant. Spectrosc. Radiat. Transfer* **51**, 113 (1994).
19. J. Delettrez, D. K. Bradley, P. A. Jaanimagi, and C. P. Verdon, *Phys. Rev. A* **41**, 5583 (1990); D. K. Bradley, J. A. Delettrez, and C. P. Verdon, *Phys. Rev. Lett.* **68**, 2774 (1992).
20. R. G. Evans, *Can. J. Phys.* **64**, 893 (1986); J. Meyer-Ter-Vehn, *Nucl. Fusion* **22**, 561 (1982); G. I. Guderley, *Luftfahrtforschung* **19**, 3032 (1942).
21. D. H. Munro, *Phys. Fluids B* **1**, 134 (1989).
22. T. Endo et al., *Phys. Rev. Lett.* **74**, 3608 (1995).
23. J. W. Jacobs and I. Catton, *J. Fluid Mech.* **187**, 329 (1988); J. W. Jacobs and I. Catton, *J. Fluid Mech.* **187**, 353 (1988).
24. R. M. Davies and G. I. Taylor, *Proc. Roy. Soc. A* **200**, 375 (1950); G. R. Baker, D. I. Meiron, and S. A. Orszag, *Phys. Fluids* **23**, 1485 (1980).
25. D. Layzer, *Astrophys. J.* **122**, 1 (1955).
26. S. W. Haan, *Phys. Fluids B* **3**, 2349 (1991).
27. D. Ofer, D. Shvartz, Z. Zinamon, and S. A. Orszag, *Phys. Fluids B* **4**, 3549 (1992).
28. E. G. Gamaly et al., *Laser Part. Beams* **8**, 173 (1990).
29. C. P. Verdon et al., *Phys. Fluids* **25**, 1653 (1982).
30. G. R. Baker, D. I. Meiron, and S. A. Orszag, *Phys. Fluids* **23**, 1485 (1980).
31. J. P. Dahlburg, J. H. Gardner, and M. H. Emery, *Bull. Am. Phys. Soc.* **35**, 1969 (1990).
32. S. W. Haan, *Phys. Rev. A* **39**, 5812 (1989).
33. E. M. Campbell, *Laser Part. Beams* **9**, 209 (1991).
34. R. J. Ellis et al., *Rev. Sci. Instrum.* **61**, 2759 (1990).
35. B. A. Remington, S. G. Glendinning, R. J. Wallace, S. Rothman, and R. Morales, *Rev. Sci. Instrum.* **63**, 5080 (1992).
36. R. Morales, B. A. Remington, T. Schwinn, *Rev. Sci. Instrum.* **66**, 700 (1995); B. A. Remington and R. I. Morales, *Rev. Sci. Instrum.* **66**, 703 (1995).
37. B. A. Remington et al., *Phys. Plasmas* **2**, 241 (1995).
38. K. S. Budil et al., "The Flexible X-Ray Imager," Lawrence Livermore National Laboratory, Livermore, CA, UCRL-JC-120837; in press, *Rev. Sci. Instrum.* (1996).
39. L. J. Suter et al., *Phys. Rev. Lett.* **73**, 2328 (1994).
40. R. L. Kauffman et al., *Phys. Rev. Lett.* **73**, 2320 (1994).
41. S. W. Haan et al., *Phys. Plasmas* **2**, 2480 (1995).
42. Ya. B. Zel'dovich and Yu. P. Raizer, *Physics of Shock Waves and High-Temperature Phenomena* (Academic, New York, 1966), Vol. I, p. 52.
43. S. P. Hatchett, Lawrence Livermore National Laboratory, Livermore, CA, UCRL-JC-108348 (1991).
44. G. B. Zimmerman and W. L. Kruer, *Comm. Plasma Phys. Controlled Fusion* **2**, 51 (1975).
45. S. V. Weber, B. A. Remington, S. W. Haan, B. G. Wilson, and J. K. Nash, *Phys. Plasmas* **1**, 3652 (1994).
46. R. M. More, K. H. Warren, D. A. Young, and G. B. Zimmerman, *Phys. Fluids* **31**, 3059 (1988).
47. K. S. Budil et al., Lawrence Livermore National Laboratory, Livermore, CA, UCRL-JC-121565 (1995); to be submitted to *Phys. Rev. Lett.*
48. B. A. Remington et al., *Phys. Rev. Lett.* **73**, 545 (1994).
49. M. J. Dunning and S. W. Haan, *Phys. Plasmas* **2**, 1669 (1995).
50. D. L. Youngs, *Physica* **12D**, 32 (1984); K. I. Read, *Physica* **12D**, 45 (1984).
51. M. M. Marinak et al., *Phys. Rev. Lett.* **75**, 3677 (1995).
52. R. J. Wallace, R. L. McEachern, and W. W. Wilcox, *ICF Quarterly Report* **4**(3), 79, Lawrence Livermore National Laboratory, Livermore, CA, UCRL-LR-105821-94-3 (1994).
53. M. M. Marinak, R. E. Tipton, B. A. Remington, et al., *ICF Quarterly Report* **5**(3), 168, Lawrence Livermore National Laboratory, Livermore, CA, UCRL-LR-105821-95-3 (1995); M. M. Marinak et al., *Phys. Plasmas*, in press (1996).
54. L. D. Landau and E. M. Lifshitz, *Fluid Mechanics*, 2nd ed. (Pergamon Press, New York, 1987), p. 180.
55. U. Alon, J. Hecht, D. Ofer, and D. Shvarts, *Phys. Rev. Lett.* **74**, 534 (1995).
56. J. P. Dahlburg et al., *Phys. Fluids B* **5**, 571 (1993).
57. T. A. Peyser et al., *Phys. Rev. Lett.* **75**, 2332 (1995); G. Dimonte et al., *Phys. Rev. Lett.* **74**, 4855 (1995).

58. J. Hecht, U. Alon, and D. Shvarts, *Phys. Fluids* **6**, 4019 (1994).
59. D. Shvarts, U. Alon, D. Ofer, R. L. McCrory, and C. P. Verdon, *Phys. Plasmas* **2**, 2465 (1995).
60. D. L. Youngs, *Phys. Fluids A* **3**, 1312 (1991); *Laser Part. Beams* **12**, 725 (1994).
61. R. P. J. Town, A. R. Bell, *Phys. Rev. Lett.* **67**, 1863 (1991).
62. G. R. Baker, R. L. McCrory, C. P. Verdon et al., *J. Fluid Mech.* **178**, 161 (1987).
63. F. Hattori, H. Takabe, and K. Mima, *Phys. Fluids* **29** (5), 1719 (1986).
64. M. A. Sweeney, F. C. Perry, *J. Appl. Phys.* **52**, 4487 (1981); J. S. Wark, J. D. Kilkenny, A. J. Cole, M. H. Key, P. T. Rumsby, *Appl. Phys. Lett.* **48**, 969 (1986); H. Nishimura, et al., *Phys. Fluids* **31**, 2875 (1988).
65. T. R. Dittrich et al., *Phys. Rev. Lett.*, **73**, 2324 (1994).
66. Y. Kato and K. Mima, *Phys. Rev. Lett.* **53**, 1057 (1984).
67. J. D. Kilkenny et al., *Rev. Sci. Instrum.* **59**, 1793 (1988); O. L. Landen et al., “Gain Uniformity, Linearity, Saturation and Depletion in Gated Microchannel-Plate X-Ray Framing Cameras,” *Ultrahigh- and High-Speed Photography, Videography, and Photonics '93*, P. W. Roehrenbecks, Ed. (SPIE, San Diego, California, 1993), Vol. 2002, pp. 2–12.
68. P. M. Bell, J. D. Kilkenny, G. Power, R. Bonner, and D. K. Bradley, in *Ultrahigh Speed and High Speed Photography, Photonics, and Videography '89*, SPIE Vol. 1155 (SPIE, Bellingham, WA, 1989), pp. 430–444.
69. J. T. Larsen, “HYADES—A Radiation Hydrodynamics Code for Dense Plasma Studies,” *4th International Workshop on Radiative Properties of Hot Dense Matter*, W. Goldstein, C. Hooper, J. Gauthier, J. Seely, R. Lee, Eds. (World Scientific, Sarasota, Florida, 1990), p. 321.